Cell

Regulation of the MEX-5 Gradient by a Spatially Segregated Kinase/Phosphatase Cycle

Erik E. Griffin,[1] David J. Odde,[2] and Geraldine Seydoux[1,*]
[1]Department of Molecular Biology and Genetics, Howard Hughes Medical Institute, Center for Cell Dynamics, Johns Hopkins School of Medicine, 725 N. Wolfe Street, PCTB 706, Baltimore, MD 21205, USA
[2]Department of Biomedical Engineering, University of Minnesota, Minneapolis, MN 55455, USA
*Correspondence: gseydoux@jhmi.edu
DOI 10.1016/j.cell.2011.08.012

SUMMARY

Protein concentration gradients encode spatial information across cells and tissues and often depend on spatially localized protein synthesis. Here, we report that a different mechanism underlies the MEX-5 gradient. MEX-5 is an RNA-binding protein that becomes distributed in a cytoplasmic gradient along the anterior-to-posterior axis of the one-cell *C. elegans* embryo. We demonstrate that the MEX-5 gradient is a direct consequence of an underlying gradient in MEX-5 diffusivity. The MEX-5 diffusion gradient arises when the PAR-1 kinase stimulates the release of MEX-5 from slow-diffusive, RNA-containing complexes in the posterior cytoplasm. PAR-1 directly phosphorylates MEX-5 and is antagonized by the spatially uniform phosphatase PP2A. Mathematical modeling and in vivo observations demonstrate that spatially segregated phosphorylation and dephosphorylation reactions are sufficient to generate stable protein concentration gradients in the cytoplasm. The principles demonstrated here apply to any spatially segregated modification cycle that affects protein diffusion and do not require protein synthesis or degradation.

INTRODUCTION

Protein gradients are an efficient way to encode spatial information within cells and across tissues. The mechanisms that generate and maintain protein gradients have been the subject of extensive theoretical and experimental analyses (Wartlick et al., 2009). Most studies have emphasized the role of a localized protein source as the foundational asymmetry underlying gradient formation. For example, in *Drosophila* embryos, the Bicoid protein is synthesized at one end of the egg from a localized pool of *bicoid* mRNA. Diffusion away from the local source and uniform protein degradation across the egg generate a concentration gradient over the course of ~2 hr (Ephrussi and St Johnston, 2004; Little et al., 2011). Extracellular gradients also depend on the localization of specialized cells that synthesize and secrete the signal (source) among cells that respond to and internalize the signal (sink) (Wartlick et al., 2009).

A spatially segregated source/sink model can also account for the formation of phosphorylation gradients or "phosphogradients." Phosphogradients have been implicated in the spatial organization of signal transduction pathways where phosphorylation modulates protein activity. Phosphogradients arise when a diffusing substrate is acted upon by a kinase (source) and phosphatase (sink) that are separated in space (Brown and Kholodenko, 1999). In phosphogradients, the ratio of unphosphorylated to phosphorylated substrate varies in space, but the overall concentration of the substrate is uniform (Brown and Kholodenko, 1999; Coppey et al., 2008; Fuller et al., 2008; Kalab et al., 2002; Maeder et al., 2007; Su et al., 1998). In 2008, Lipkow and Odde predicted that, if phosphorylation changes the diffusivity of the substrate, spatially segregated kinase/phosphatase cycles would also affect the *overall* distribution of the substrate to generate a protein concentration gradient (Lipkow and Odde, 2008). The spatial bias in the generation of the phosphorylated isoform generates a diffusion gradient that causes the substrate to concentrate in regions of low diffusivity (Lipkow and Odde, 2008). In the present study, we provide experimental evidence in support of this model in *C. elegans*.

The *C. elegans* one-cell embryo (zygote) is a classic model for the study of intracellular asymmetries (Goldstein and Macara, 2007; St Johnston and Ahringer, 2010). After fertilization, a group of conserved polarity regulators, the PAR proteins, sort into anterior (PAR-3/PAR-6/PKC-3) and posterior (PAR-2 and PAR-1) domains in the actin-rich layer (or "cortex") under the plasma membrane (Kemphues, 2000). In response to PAR asymmetry at the cortex, cell-fate determinants become asymmetrically distributed in the cytoplasm. Among them is the RNA-binding protein MEX-5, which redistributes in 10 min into an anterior-high/posterior-low gradient across the length of the 50 μm zygote (Schubert et al., 2000; Tenlen et al., 2008). MEX-5, in turn, partitions other factors such as PIE-1 to the posterior cytoplasm and PLK-1 to the anterior cytoplasm (Budirahardja and Gönczy, 2008; Mello et al., 1996; Rivers et al., 2008; Schubert et al., 2000). Consequently, during the first cell division, the two daughter blastomeres inherit different determinants, which

help to specify their distinct fates (anterior/somatic and posterior/germline). Mutations in the PARs cause MEX-5 (and its targets) to remain symmetrically distributed (Schubert et al., 2000; Tenlen et al., 2008), but the mechanisms linking PAR asymmetry to the MEX-5 gradient are not known.

Fluorescence recovery after photobleaching (FRAP) and fluorescence correlation spectroscopy (FCS) experiments have shown that, in polarized zygotes, GFP::MEX-5 diffuses faster in the posterior cytoplasm, where MEX-5 protein concentration is lowest (Daniels et al., 2010; Tenlen et al., 2008). Fast diffusion requires *par-1* activity and a C-terminal serine in MEX-5 (S458), which is phosphorylated in a *par-1*- and *par-4*-dependent manner in vivo (Tenlen et al., 2008). Phosphorylation of S458, however, does not correlate with gradient formation or fast diffusion, suggesting that other mechanisms regulate MEX-5 asymmetry (Tenlen et al., 2008). Two speculative models have been proposed. The first model invokes dynamic binding of MEX-5 to cytoskeletal elements asymmetrically distributed in the cytoplasm (Tenlen et al., 2008). In this model, the PARs localize MEX-5 indirectly by localizing factors, such as myosin, that retard MEX-5 diffusion in the anterior cytoplasm (Tenlen et al., 2008). A second model proposes that the PARs regulate MEX-5 distribution by forming "reactive surfaces" in the anterior and posterior cortices, which locally decrease and increase, respectively, the rate of MEX-5 diffusion (Daniels et al., 2010). How the PARs modify MEX-5 diffusion, and how differences originated at the cortex are propagated through the cytoplasm, however, is not known.

In this study, we present evidence that the MEX-5 gradient arises as a direct consequence of a complementary PAR-1 kinase activity gradient in the cytoplasm. We demonstrate that MEX-5 is a substrate of PAR-1 and identify PP2A as the opposing phosphatase in the cytoplasm. Our findings reveal an unexpected direct patterning role for PAR-1 in the cytoplasm and provide experimental evidence for the theoretical model of Lipkow and Odde (2008).

RESULTS

A MEX-5 Diffusion Gradient Underlies the MEX-5 Concentration Gradient

To examine MEX-5 dynamics in live zygotes, we generated a Dendra::MEX-5 fusion. Dendra is a photoactivatable fluorescent protein that is photoconverted irreversibly from green to red fluorescence by exposure to 405 nm light (Gurskaya et al., 2006). Unlike FRAP, photoconversion is a positive marking technique that can be used to measure rates of protein degradation and diffusion, without interference from new protein synthesis (Lippincott-Schwartz and Patterson, 2008). We first photoconverted Dendra::MEX-5 throughout the zygote before polarization (prior to appearance of the pronuclei). We found that photoconverted Dendra::MEX-5 (Dendra^{R}::MEX-5) formed an ~3-fold anterior-posterior gradient by nuclear envelope breakdown (NEBD, first mitotic division), as is observed for endogenous MEX-5 (Figures 1A and 1B). Total levels of Dendra^{R}::MEX-5 did not change during gradient formation: levels increased in the anterior half and decreased in the posterior half by ~25% (Figure 1C). We conclude that formation of the MEX-5 gradient involves redistribution of existing MEX-5 and does not require MEX-5 synthesis or degradation.

Next, to compare mobility of MEX-5 between the anterior and posterior, we photoconverted Dendra::MEX-5 in two stripes at ~30% and ~70% embryo length during polarization (Figure 1D). Dendra^{R}::MEX-5 diffused symmetrically away from both stripes with no directional bias (Figure 1D). The apparent diffusivity of Dendra^{R}:MEX-5, however, appeared to differ between the two stripes, with faster diffusion in the posterior stripe (Figure 1D). These observations are consistent with earlier FRAP experiments, which showed that GFP::MEX-5 diffuses faster in the posterior cytoplasm after polarization (Daniels et al., 2010; Tenlen et al., 2008).

To examine MEX-5 mobility systematically during polarization, we measured the apparent diffusion coefficient (D_c) of Dendra^{R}::MEX-5 at 17 positions along the long (anterior-posterior) axis and 3 positions along the short axis, before polarization (before pronuclear formation), at the onset of polarization (pronuclear formation), and after polarization (NEBD). The apparent D_c of Dendra^{R}::MEX-5 was uniformly slow before pronuclear formation (average D_c between 10% and 90% embryo length was 0.78 $\mu m^2/s$) (Figure 1E). After pronuclear formation, the apparent D_c of Dendra^{R}::MEX-5 increased to an average of 1.70 $\mu m^2/s$. This increase was observed throughout the central cytoplasm, but not in the cytoplasm nearest the cortex (peripheral cytoplasm) where Dendra^{R}::MEX-5 diffusion remained slow (Figure 1E). By NEBD, the apparent D_c of Dendra^{R}::MEX-5 was graded linearly throughout the cytoplasm, with the lowest value at the anterior-most position and the highest value at the posterior-most position, mirroring the MEX-5 protein concentration gradient (compare Figures 1B and 1E). We conclude that redistribution of MEX-5 correlates temporally and spatially with changes in MEX-5 diffusion.

par-1 Is Necessary and Sufficient to Increase MEX-5 Diffusion in Zygotes

To determine whether the anterior or posterior PARs regulate MEX-5 dynamics, we monitored MEX-5 distribution and diffusion at NEBD in zygotes defective for the anterior kinase aPKC/PKC-3 or the posterior kinase PAR-1 (Figure 2A). *pkc-3(RNAi)* embryos lack PKC-3 and have uniform PAR-1 (Figure 2A and Figure S1A available online). The *par-1* allele *it51* inactivates PAR-1 kinase activity but does not affect PAR-1 or PKC-3 localizations (Figures 2A and 2B; Figure S1B) (Cheeks et al., 2004; Guo and Kemphues, 1995). Previous work has shown that in *par-1(RNAi)* embryos, MEX-5 mobility does not increase in the posterior cytoplasm and MEX-5 does not segregate (Tenlen et al., 2008). We found that Dendra^{R}::MEX-5 remained symmetrically distributed in both *pkc-3(RNAi)* and *par-1(it51)* zygotes (Figures S1A and S1B). Strikingly, the apparent D_c of Dendra^{R}::MEX-5 was uniformly high in *pkc-3(RNAi)* zygotes and uniformly low in *par-1(it51)* and *par-1(it51);pkc-3(RNAi)* zygotes (Figure 2C). We conclude that PAR-1 functions downstream of PKC-3 and is required to stimulate MEX-5 diffusion.

In polarized zygotes, PAR-1 kinase is present both in the cytoplasm and on the posterior cortex (Guo and Kemphues, 1995). To examine PAR-1 dynamics during polarization, we imaged zygotes expressing a full-length GFP::PAR-1 fusion. Before

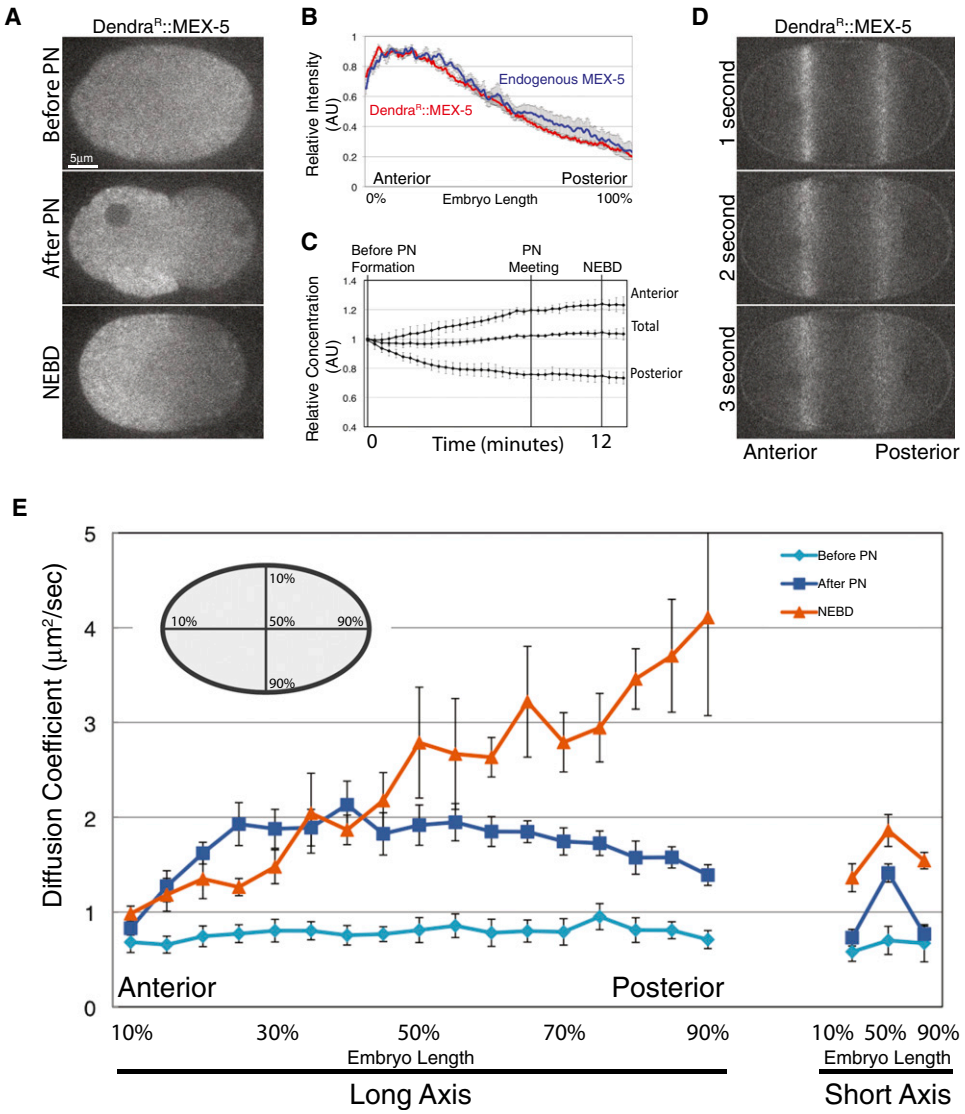

Figure 1. A Gradient in Diffusivity Underlies the MEX-5 Gradient

(A) Time-lapse photomicrographs of a zygote expressing Dendra::MEX-5 photoconverted before pronuclear formation (before polarization). All embryos in this and subsequent figures are oriented with anterior to the left and posterior to the right. PN stands for pronuclear formation, which marks the onset of polarity. NEBD stands for nuclear envelope breakdown (mitosis) and occurs 10 min after pronuclear formation, by which time MEX-5 is maximally polarized.

(B) Graph plotting the relative signal intensity of Dendra^R::MEX-5 (red line; n = 7 embryos) and endogenous MEX-5 (blue line; n = 5 embryos) along the long axis of the zygote after NEBD. Fluorescence intensity was averaged along a 20 pixel-wide box spanning the length of each zygote (0% anterior-most pole, 100% posterior-most pole). Maximum values for each zygote were normalized to 1. Error bars represent the standard error of the mean (SEM).

(C) The relative concentration of Dendra^R::MEX-5 was measured in the anterior half, in the posterior half, and throughout the zygote (total) from before pronuclear formation to 1 min following NEBD (just prior to cytokinesis). Mid-plane images were collected every 20 s. Embryos were normalized to each other by setting the initial total value to 1 and averaged together (n = 5 embryos). Error bars represent SEM.

(D) Time-lapse photomicrographs of a zygote during polarity establishment (pronuclear migration) expressing Dendra::MEX-5 photoactivated in two stripes. Time since photoactivation is indicated. Note that the signal from the posterior stripe diffuses more rapidly.

(E) Plot showing the apparent diffusion coefficient (D_c) of Dendra^R::MEX-5 at different positions along the long and short axes of the zygote and at different stages. Embryo schematic shows the position of the photoconversion stripes along the long and short axes. "Peripheral cytoplasm" as mentioned in the text refers to 10% and 90% embryo length. Error bars represent SEM.

pronuclear formation, GFP::PAR-1 was uniformly distributed in the cytoplasm and weakly on the cortex (data not shown). At pronuclear formation, GFP::PAR-1 levels increased in the central cytoplasm and decreased in the peripheral cytoplasm (Figure 2D). This relocalization coincided temporally and spatially with an increase in Dendra^R::MEX-5 diffusion in the central cytoplasm (Figure 1E) and an increase in Dendra^R::MEX-5 levels in the peripheral cytoplasm (Figure 2D). During pronuclear

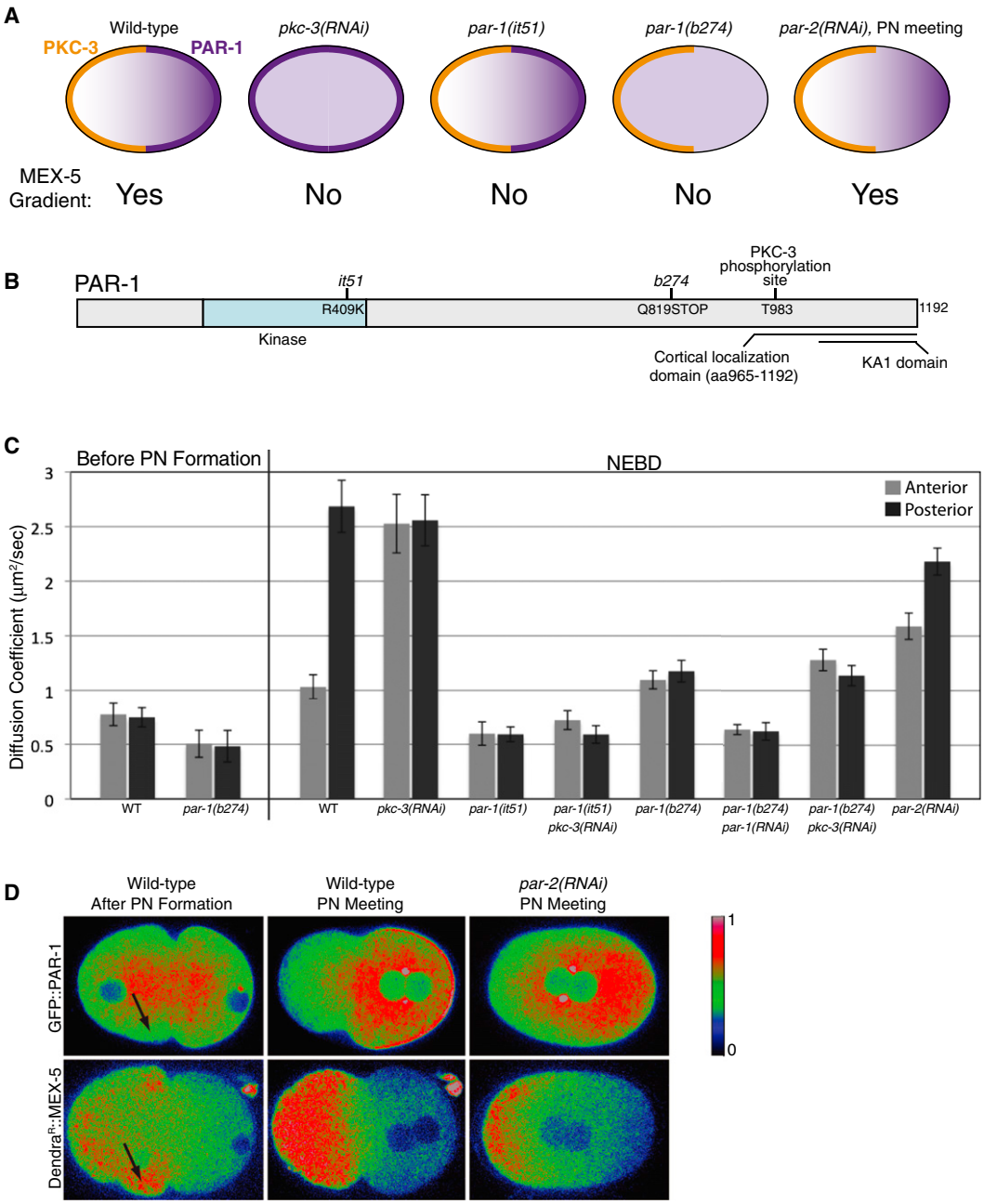

Figure 2. PAR-1 Is Necessary and Sufficient to Increase MEX-5 Mobility

(A) Diagrams showing the distributions of PKC-3 (orange) and PAR-1 (purple on cortex and in cytoplasm) in zygotes of the indicated genotypes. MEX-5 localizes in a gradient in wild-type and *par-2(RNAi)* embryos and remains symmetrically distributed in all other genotypes. *par-1(it51)* and *par-1(b274)* are mutations that, respectively, inactivate PAR-1 kinase activity and truncate the PAR-1 protein (Figure S1E) (Guo and Kemphues, 1995). Also see Figures S1A, S1B, and S1E.

(B) PAR-1 schematic: T983 is a conserved aPKC/PKC-3 phosphorylation site. The C-terminal domain (965–1192) contains the lipid-binding domain KA1 (Moravcevic et al., 2010) and localizes in a cytoplasmic gradient and to the posterior cortex (E.E.G., A.A. Cuenca, and G.S., unpublished data).

(C) Apparent D_c of Dendra^R::MEX-5 measured in the anterior (25% embryo length) and posterior (75% embryo length) cytoplasm in zygotes of the indicated genotypes. Error bars represent SEM.

(D) Comparison of the distribution of GFP::PAR-1 and Dendra^R::MEX-5 in wild-type and *par-2(RNAi)* zygotes. Fluorescence intensity is represented by a rainbow scale ranging from blue (low signal intensity) to red (high signal intensity). Arrows point to the subcortical region where GFP::PAR-1 is depleted and Dendra^R::MEX-5 accumulates after pronuclear formation. Note that in *par-2(RNAi)* zygotes, GFP::PAR-1 does not accumulate on the posterior cortex but still forms a cytoplasmic gradient.

Also see Figures S1C, S1D, and S1F.

migration, GFP::PAR-1 levels remained low in the anterior-peripheral cytoplasm but increased in the posterior cytoplasm and on the posterior cortex. By NEBD, GFP::PAR-1 was enriched on the posterior cortex and formed a 3-fold anterior-low/posterior-high gradient in the cytoplasm, paralleling the gradient in MEX-5 diffusivity (Figure 2D and Figure S1C). Immunostaining of wild-type (WT) embryos with an anti-PAR-1 antibody confirmed the presence of a PAR-1 gradient in the cytoplasm of zygotes at NEBD (Figure S1D). We conclude that PAR-1 dynamics in the cytoplasm correlate with MEX-5 diffusion dynamics and that MEX-5 responds quickly to changes in PAR-1 distribution.

To explore whether cytoplasmic PAR-1 is sufficient to stimulate MEX-5 diffusion, we analyzed the *par-1* allele *b274*. *par-1(b274)* zygotes do not localize PAR-1 to the cortex and do not segregate MEX-5 but are positive for pS458, suggesting that this allele retains some *par-1* kinase activity (Figure S1B) (Guo and Kemphues, 1995; Tenlen et al., 2008). We sequenced *par-1(b274)* and found a premature stop codon at residue Q819 between the kinase domain and the domain that localizes PAR-1 to the cortex (Figure 2B). Western blotting and immunofluorescence analyses confirmed the presence of a truncated PAR-1 protein, expressed at 14% of wild-type levels and uniformly cytoplasmic (Figures S1B and S1E) (Hurd and Kemphues, 2003). Before pronuclear formation, Dendra^R::MEX-5 mobility was uniformly low in *par-1(b274)* zygotes, as in wild-type and *par-1(it51)* zygotes. By NEBD, however, the apparent D_c of Dendra^R::MEX-5 had increased throughout the cytoplasm to a value intermediate between that of *par-1(it51)* and *pkc-3(RNAi)* zygotes (Figure 2C). In *par-1(b274)* zygotes, PKC-3 became enriched on the anterior cortex as in wild-type, whereas Dendra^R::MEX-5 remained symmetrically distributed (Figure S1B) (Tenlen et al., 2008). The intermediate Dendra^R::MEX-5 diffusion rate in *par-1(b274)* zygotes was dependent on PAR-1 but not on PKC-3 (Figure 2C). We conclude that PAR-1 kinase activity in the cytoplasm is sufficient to increase MEX-5 diffusivity after pronuclear formation.

We also examined the distribution of PAR-1 and MEX-5 in *par-2* zygotes, which localize anterior PARs to the anterior cortex before, but not after, NEBD and which never enrich PAR-1 on the posterior cortex (Boyd et al., 1996; Cuenca et al., 2003). We found that GFP::PAR-1 still formed a cytoplasmic gradient by pronuclear meeting in *par-2(RNAi)* zygotes (Figure 2D and Figure S1C). The GFP::PAR-1 gradient was transient and became less pronounced following NEBD (Figure S1C). Remarkably, Dendra^R::MEX-5 also formed a gradient by pronuclear meeting, which weakened following NEBD (Figure 2D and Figure S1F). The diffusivity of Dendra^R::MEX-5 was also asymmetric in *par-2(RNAi)* zygotes (Figure 2C). We conclude that formation of a cytoplasmic PAR-1 gradient is sufficient to change MEX-5 diffusion and drive the formation of a complementary MEX-5 gradient.

PAR-1 Phosphorylates MEX-5 on Two Residues: S458 and S404

Phosphorylation of S458 depends on *par-1* activity in vivo, raising the possibility that MEX-5 is a PAR-1 substrate (Tenlen et al., 2008). To test this possibility directly, we expressed the PAR-1 kinase domain (aa 1–492) fused to maltose-binding protein (MBP) in *E. coli*. We also included the activating mutation T325E in the kinase activation loop (Lizcano et al., 2004). MBP:PAR-1(aa 1–492, T325E) phosphorylated MBP:MEX-5, but not MBP or MBP:PIE-1 (Figure 3A). Replacement of S458 with alanine reduced, but did not abolish, phosphorylation of MBP:MEX-5 (Figure 3A). Using a combination of deletion and alanine mutagenesis, we identified S404 as a second PAR-1 phosphorylation site in MEX-5 (Figure 3A). MEX-5 mutated at both S404 and S458 was no longer a substrate for MBP:PAR-1 (aa 1–492, T325E) (Figure 3A). To determine whether S404 is phosphorylated by PAR-1 in vivo, we generated an antibody specific for pS404 (Figure S2A). Anti-pS404 immunoprecipitated ~5% of total MEX-5 from extracts prepared from wild-type hermaphrodites and only ~1.7% from extracts prepared from *par-1(RNAi)* hermaphrodites (Figure 3B). We conclude that PAR-1 phosphorylates MEX-5 on S458 and S404 in vitro and in vivo.

Reversible Phosphorylation of S404 Is Required to Form the MEX-5 Gradient

To investigate the role of S404 and S458 phosphorylation in vivo, we examined the distribution of MEX-5(S404A) and MEX-5(S458A) fusions. As reported in Tenlen et al. (2008), the distribution of MEX-5(S458A) was variable from embryo to embryo, with a minority of embryos forming a shallow MEX-5 gradient. In contrast, Dendra^R::MEX-5(S404A) was symmetrically distributed in all embryos examined (Figure 3C). The double mutant S404A/S458A behaved like S404A (data not shown). Dendra^R::MEX-5(S404A) diffusion was slow, comparable to that of wild-type Dendra^R::MEX-5 in *par-1(it51)* (Figure 3D and Figure 2C). Dendra^R::MEX-5(S404A) remained slow diffusing in *pkc-3(RNAi)* and in *par-1(b274)* zygotes, indicating that this fusion is no longer sensitive to changes in PAR-1 activity or localization (Figure 3D). We conclude that the MEX-5 protein and diffusivity gradients depend primarily on phosphorylation of S404 by PAR-1.

Immunofluorescence experiments using a phosphospecific antibody have shown that S458 is phosphorylated during oogenesis, and MEX-5 phosphorylated on S458 becomes enriched in the anterior in zygotes as does total MEX-5 (Tenlen et al., 2008). These observations suggest that pS458 is relatively stable and does not respond to changes in PAR-1 localization during polarization. In contrast, we were not able to visualize pS404 by immunofluorescence, even though our phosphospecific antibody could immunoprecipitate MEX-5 from extracts (Figure 3B). We detected pS404 in extracts from *fem-3(e2006)* females, which contain oocytes but no embryos, suggesting that like S458, S404 is already phosphorylated during oogenesis (data not shown). To examine phosphorylation and dephosphorylation dynamics at S458 and S404, we phosphorylated MEX-5 in vitro using MBP::PAR-1(aa 1–492; T325E) and incubated phosphorylated MEX-5 with embryo extract. Although both sites were phosphorylated at similar rates in vitro, S404 was dephosphorylated significantly faster than S458 in embryo extracts (Figure 3E). Dephosphorylation was inhibited by 200 nM okadaic acid, consistent with the presence of phosphatases in the extract (Figure 3E). We conclude that embryos

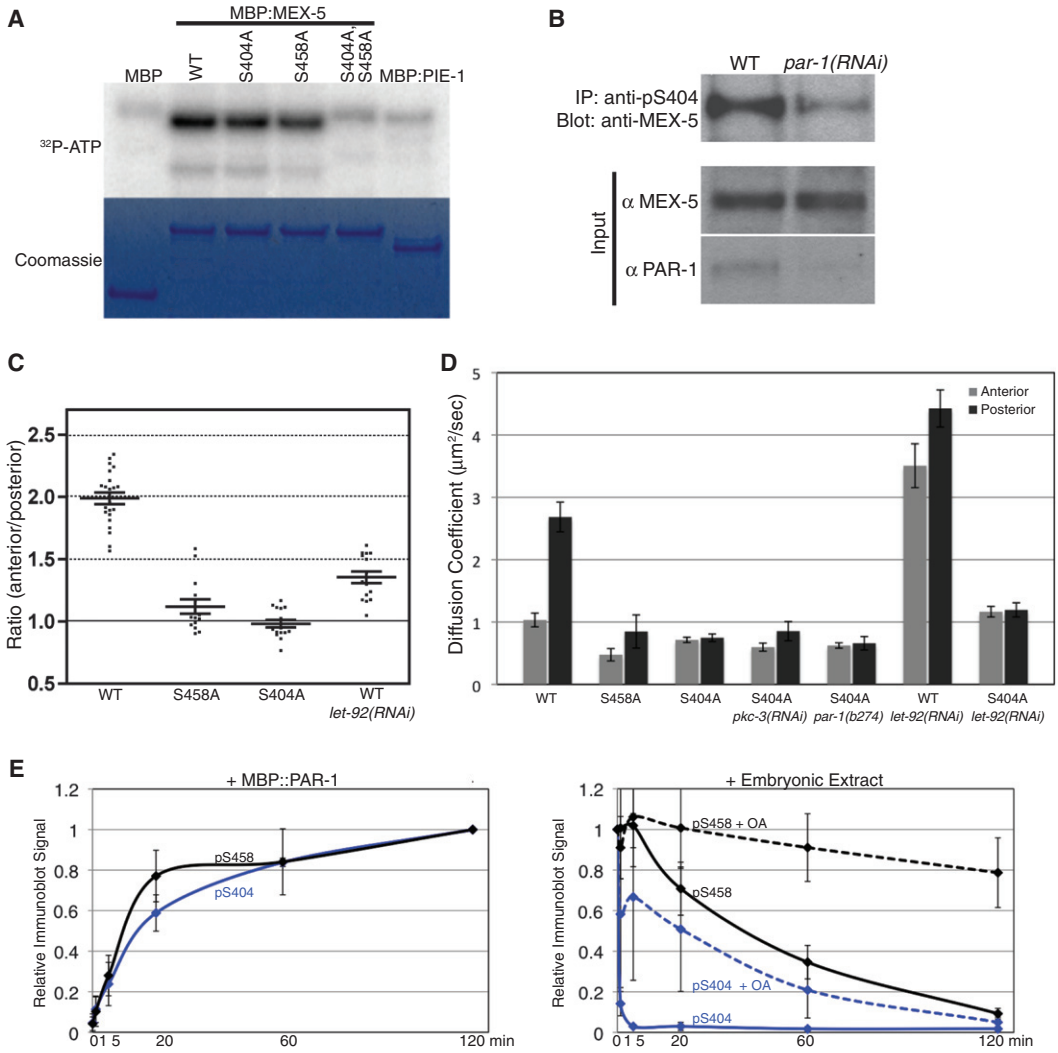

Figure 3. PAR-1 Phosphorylates MEX-5 on S404 In Vitro and In Vivo

(A) SDS-PAGE gel of kinase reactions using MBP:PAR-1(aa 1–492; T325E) and the indicated MBP substrates. Reactions were performed in the presence of [^{32}P]-ATP for 30 min. Top panel shows [^{32}P] incorporation and bottom panel is Coomassie blue staining of the same gel.

(B) Western blot analysis of immunoprecipitates from whole worm extracts obtained with anti-MEX-5 pS404 antibodies. Five percent of extract used for immunoprecipitation was loaded in input lanes. In the bottom panel, extract was probed with anti-PAR-1 antibodies to demonstrate depletion by *par-1(RNAi)*.

(C) Ratio of mean anterior and posterior fluorescence intensities for embryos expressing the indicated Dendra^{R}::MEX-5 fusions at NEBD. Each dot represents an individual embryo. Long bars represents the mean ratio and short bars represent the SEM.

(D) Apparent D_c of Dendra^{R}::MEX-5 mutants at NEBD. Dendra::MEX-5 was photoconverted along the anterior-posterior axis and apparent D_c was calculated at 25% (anterior) and 75% (posterior) embryo length. Error bars represent SEM. The results for wild-type embryos are also displayed in Figure 2C and Figure 4D. Also see Figures S2B and S2C.

(E) Dynamics of pS404 and pS458 in vitro. *Left panel:* MBP:MEX-5 was incubated with MBP:PAR-1(aa 1–492; T325E) and analyzed by western blot with phosphospecific pS458 and pS404 antibodies at the indicated times. *Right panel:* Phosphorylated MBP::MEX-5 was incubated with embryonic extract in the presence or absence of 200 nM okadaic acid (+ OA) and analyzed by western blot with pS404 and pS458 phosphospecific antibodies. Note the rapid dephosphorylation at S404. Error bars represent SEM. Also see Figure S2A.

contain a phosphatase activity that efficiently reverses S404 phosphorylation.

The okadaic acid-sensitive phosphatase PP2A has been implicated as a PAR-1 antagonist in *Drosophila* and *C. elegans* (Kao et al., 2004; Krahn et al., 2009; Nam et al., 2007; Yoder et al., 2004). PP2A is a heterotrimeric phosphatase consisting of structural, catalytic, and regulatory subunits. In *C. elegans*, the catalytic subunit, LET-92, is distributed throughout the cytoplasm, on centrosomes, and on P granules (Schlaitz et al., 2007). To test whether PP2A influences MEX-5 dynamics, we analyzed *let-92(RNAi)* embryos. *let-92(RNAi)* increased the mobility and decreased the asymmetry of wild-type Dendra^{R}::MEX-5 (Figures 3C and 3D). Consistent with PP2A acting primarily via S404, *let-92(RNAi)* only slightly increased the

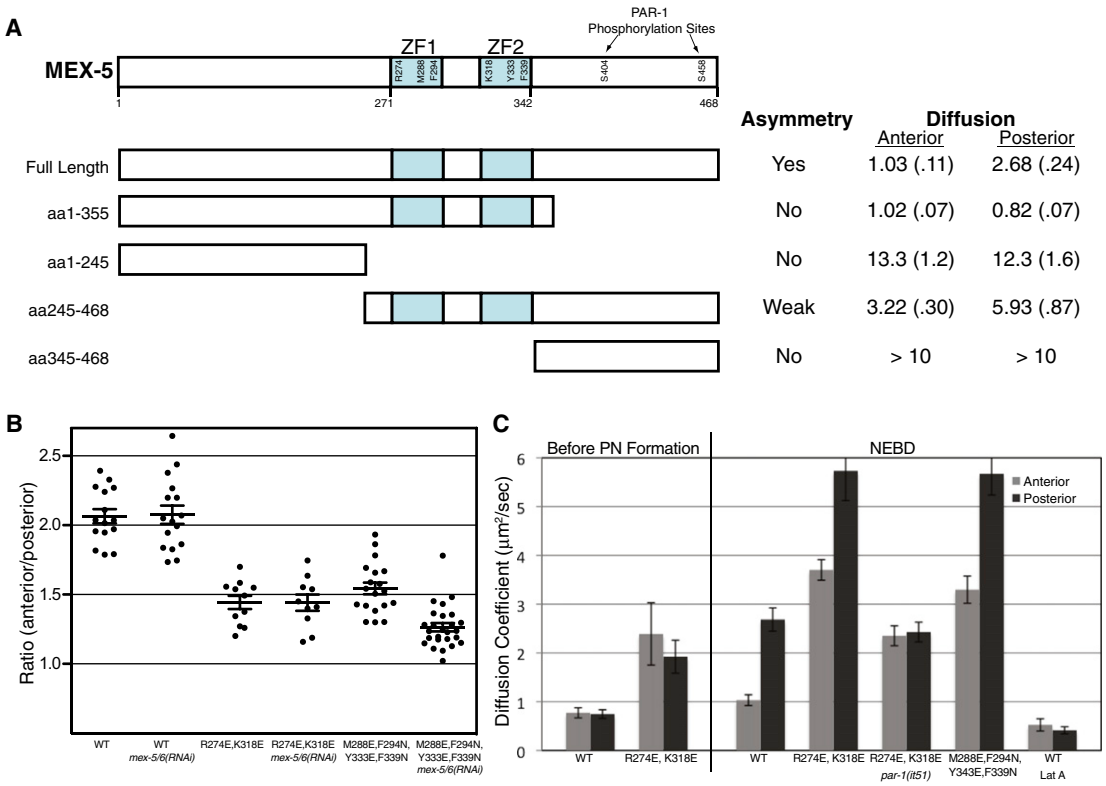

Figure 4. Regulation of MEX-5 Mobility by RNA Binding

(A) Schematic showing the MEX-5 truncations. Each construct was expressed as a Dendra fusion and its localization and apparent D_c ($\mu m^2/s$) were determined at NEBD (SEM in parentheses). The apparent D_c of Dendra^R::MEX-5(aa 345–468) could not be determined accurately because of its rapid diffusion and relatively low expression but exceeded 10 $\mu m^2/s$.

(B) Ratio of anterior and posterior fluorescence intensities for embryos expressing the indicated Dendra::MEX-5 fusions. Each dot represents an individual embryo. Long bars represent the mean ratio and short bars represent SEM.

(C) Apparent D_c of Dendra^R::MEX-5 mutants measured before pronuclear (PN) formation (before polarization) and at NEBD (after polarization). The results for wild-type embryos are also presented in Figure 2C and Figure 3D. Error bars represent SEM.

See also Figure S3.

mobility of Dendra^R::MEX-5 (S404A) (Figure 3D). *let-92(RNAi)* did not affect the posterior localization of PAR-1 (Figures S2B and S2C). We conclude that PP2A, and possibly other phosphatases, antagonizes PAR-1-dependent phosphorylation of MEX-5 to return MEX-5 to a slow-diffusing state.

RNA Binding Limits MEX-5 Diffusion

The apparent D_c of Dendra^R::MEX-5 before and after polarization is 10- to 20-fold lower than that of Dendra^R alone (data not shown). To determine which domains of MEX-5 retard its mobility, we compared the localization and diffusion behavior of a Dendra::MEX-5 deletion series (Figure 4A). A C-terminal truncation lacking S404 and S458 (Dendra::MEX-5(aa 1–355)) was symmetrically distributed and uniformly slow diffusing even after polarization of the zygote (Figure 4A). An N-terminal truncation (Dendra^R::MEX-5(aa 245–468)) showed a moderate increase in mobility in the anterior and posterior cytoplasm and a shallower but still detectable gradient (Figure 4A). In contrast, fusions lacking the CCCH fingers (Dendra^R::MEX-5(aa 1–244) and Dendra^R::MEX-5(aa 345–468)) diffused >10 times faster and lacked all asymmetry (Figure 4A). Consistent with these findings, a GFP::MEX-5 fusion lacking only the CCCH fingers was uniformly distributed and fast diffusing (Tenlen et al., 2008). We conclude that MEX-5 localization and slow mobility depend primarily on the CCCH fingers, with an additional contribution from the N-terminal domain.

The CCCH fingers of MEX-5 mediate RNA binding in vitro (Pagano et al., 2007). To test whether RNA binding retards MEX-5 mobility, we examined missense mutations in the CCCH fingers. Studies on the TIS11 family of CCCH finger proteins identified key amino acids that contact RNA, mutations in which disrupt RNA binding (Hudson et al., 2004; Lai et al., 2002). The corresponding mutations in MEX-5 are M288E, M294N, Y333E, F339N. In vitro, MEX-5 binds preferentially to poly-U tracks, a sequence common in *C. elegans* 3′ UTRs (Pagano et al., 2007). R274E and K318E decrease MEX-5 affinity for poly-U by 35-fold but only modestly reduce MEX-5 ability to bind to a related sequence (UUAUUUAUU) (Pagano et al., 2007). We found that both Dendra^R::MEX-5(M288E, M294N, Y333E, F339N) and Dendra^R::MEX-5 (R274E, K318E) formed a shallower gradient than wild-type and exhibited increased diffusivity in both the anterior and posterior (Figures 4B and 4C). The

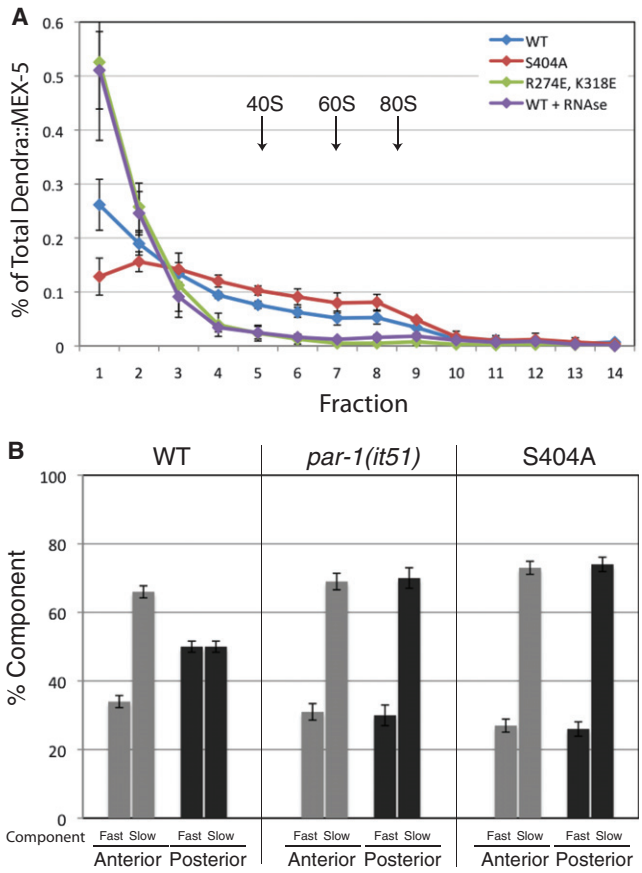

Figure 5. MEX-5 Associates with Multiple Complexes In Vivo

(A) Distribution of Dendra::MEX-5 fusions following sucrose gradient fractionation and detection by anti-Dendra western blot. Light fractions are on the left and heavy fractions are on the right. Approximate positions of the 40S, 60S, and 80S ribosomal subunits are indicated. Error bars represent SEM. See Figure S4A for UV trace.

(B) Percentage of fast and slow MEX-5 complexes detected by FCS. Note that fast and slow components were detected in all measurements. Error bars represent SEM (wild-type, n = 24, *par-1(it51)*, n = 5; S404A, n = 8 embryos). See Figures S4B and S4C.

apparent D_c of Dendra^R::MEX-5 (R274E, K318E) was reduced in *par-1(RNAi)* but remained higher than wild-type MEX-5, indicating that Dendra^R::MEX-5 (R274E, K318E) is still regulated by PAR-1 but is intrinsically more mobile than wild-type Dendra^R::MEX-5 (Figure 4C). We conclude that RNA binding retards MEX-5 mobility.

Tenlen et al. (2008) reported that cysteine-to-serine substitutions predicted to disrupt folding of the CCCH fingers do not affect the MEX-5 gradient (Tenlen et al., 2008). We also found that Dendra^R::MEX-5(C286S,C292S,C331S,C337S) forms a gradient similar to wild-type Dendra^R::MEX-5. Dendra^R::MEX-5(C286S,C292S,C331S,C337S), however, diffused faster than Dendra^R::MEX-5 and was dependent on endogenous wild-type MEX-5 and MEX-6 to form a gradient (Figures S3A and S3B) (Tenlen et al., 2008). In contrast, the diffusive behaviors of Dendra^R::MEX-5(WT) and Dendra^R::MEX-5(R274E, K318E) were not dependent on endogenous MEX-5 or MEX-6 (Figure 4B). These observations suggest that, in addition to RNA binding, interactions among MEX-5 and MEX-6 molecules can also contribute to MEX-5's diffusive behavior.

The actin cytoskeleton, which becomes enriched in the anterior cytoplasm during polarization, has been proposed as another candidate for retarding MEX-5 mobility (Tenlen et al., 2008). To test this possibility, we treated zygotes with Latrunculin A, which depolymerizes F-actin and blocks polarization of the PARs (Severson and Bowerman, 2003). Latrunculin A treatment resulted in uniformly slow MEX-5 diffusion and blocked Dendra^R::MEX-5 gradient formation (Figure 4C and data not shown), indicating that F-actin is not essential to retard MEX-5 mobility.

MEX-5 Associates with Large Complexes in an RNA-Dependent Manner

To directly investigate whether MEX-5 associates with RNA in vivo, we examined the distribution of Dendra::MEX-5 in worm extracts fractionated on a 10%–45% sucrose gradient. Dendra::MEX-5 was detected in both light and heavy fractions, including fractions containing 80S ribosomes (fractions 8 and 9, Figure 5A and Figure S4A). In contrast, Dendra alone was found primarily in the lightest fractions (Figure S4A). RNase treatment that eliminated the polysome RNA peaks, but not the 80S peaks, caused the Dendra::MEX-5 to shift toward the lighter fractions, indicating that the association of MEX-5 with large complexes is RNA dependent (Figure 5A and Figure S4A).

To test whether MEX-5's behavior on sucrose gradients correlates with MEX-5's diffusive behavior in vivo, we examined Dendra::MEX-5(R274E, K318E) and Dendra::MEX-5(S404A). We found that the profile of the fast-diffusing Dendra::MEX-5(R274E, K318E) was shifted toward the lighter fraction, whereas the profile of slow-diffusing MEX-5(S404A) was shifted toward the heavy fractions (Figure 5A and Figure S4A). We conclude that MEX-5 exists in both light and heavy complexes, and that association with the latter depends on RNA and correlates with slower diffusion.

MEX-5 Exists in Multiple Diffusive Complexes In Vivo

The broad distribution of MEX-5 in sucrose gradients suggests that MEX-5 exists in multiple complexes in vivo. To test this hypothesis directly, we used fluorescence correlation spectroscopy (FCS) to measure the diffusive behavior of individual GFP::MEX-5 molecules in live zygotes. We monitored GFP::MEX-5 at 30% and 70% embryo length in 24 zygotes at NEBD. Autocorrelation curves were fit to three-dimensional models containing one, two, or three diffusive components. One-component models yielded D_c values that were significantly slower than observed with Dendra^R::MEX-5 in both the anterior and posterior (anterior = 0.26 ± 0.05 $\mu m^2/s$; posterior = 0.37 ± 0.1 $\mu m^2/s$) (Figure S4B). Two-component models yielded fast and slow components with ~100-fold difference in D_c values, whose weighted averages (an estimate of the population D_c) were in good agreement with those observed with Dendra^R::MEX-5 (anterior = 1.40 ± 0.29 $\mu m^2/s$; posterior = 3.13 ± 0.37 $\mu m^2/s$) (Figures S4B and S4C). The concentration ratio of slow:fast components was significantly higher in the anterior cytoplasm (66:34) compared to the posterior cytoplasm (50:50) (Figure 5B). We conclude that, as

suggested by the sucrose gradients, MEX-5 exists in multiple complexes in the cytoplasm, with a bias toward slower complexes in the anterior.

To examine the effect of phosphorylation by PAR-1, we repeated the FCS measurements in *par-1(it51)* zygotes and in wild-type zygotes expressing MEX-5(S404A). We obtained similar FCS profiles for both genotypes. As described above for wild-type GFP::MEX-5, one-component models yielded D_c values that were significantly lower than those observed with Dendra^R:MEX-5 in *par-1(it51)* embryos or Dendra^R::MEX-5(S404A) in wild-type embryos (Figure S4B). Two-component models, in contrast, yielded D_c values consistent with the Dendra^R values (Figure 5B and Figure S4B). The D_c and concentration ratios of fast and slow complexes were similar to those observed in the anterior of wild-type embryos (Figure 5B and Figure S4C). These results suggest that MEX-5 distributes between slow- and fast-diffusing complexes even in the absence of PAR-1, and that phosphorylation by PAR-1 shifts the distribution of MEX-5 in favor of faster complexes.

Our FCS results indicate that MEX-5 fast and slow complexes exhibit dramatically different rates of diffusion: 5.15 $\mu m^2/s$ (10–90th percentile range of 1.73 to 10.7 $\mu m^2/s$) for the fast class, and 0.086 $\mu m^2/s$ (10–90th percentile range of 0.025 to 0.16 $\mu m^2/s$) for the slow class. Daniels et al. (2010) reported a similar range of mobilities for wild-type MEX-5 but did not report the relative concentration of the slowest species and only considered species within the fast range in their modeling of the MEX-5 gradient (Daniels et al., 2010). Our analysis, however, indicates that the slow species contributes significantly to the overall diffusive behavior of MEX-5 (~70% of MEX-5 complexes in the anterior). Omission of the slow-diffusing species when calculating population D_c yields values that do not match those observed experimentally using photoactivation (this work) or FRAP (Daniels et al., 2010). We conclude that the slow-diffusing species cannot be excluded from a description of MEX-5's diffusive behavior.

Modeling of the MEX-5 Gradient

To determine whether our experimental results can be integrated into a self-consistent theoretical framework, we developed a mathematical model for the reaction-diffusion dynamics of MEX-5 (Figure 6A). The model is based on the principle that steady-state protein gradients form if (1) different phosphostates exhibit different diffusion coefficients and (2) interconversion between phosphostates is mediated by spatially segregated kinase and phosphatase reactions (Lipkow and Odde, 2008). We approximated MEX-5 diffusion dynamics by allowing for a fast species (D_{fast} = 5 $\mu m^2/s$) and a slow species (D_{slow} = 0.07 $\mu m^2/s$) whose interconversion is regulated by a phosphorylation cycle mediated by PAR-1 and PP2A (and possibly other phosphatases) (Figure 6A). Because the relative activity of cortical and cytoplasmic PAR-1 are not known, we independently considered how cytoplasmic and cortical PAR-1 affect MEX-5 segregation. Phosphatase activity was assumed to be uniform in the cytoplasm such that, in both scenarios, the kinase and phosphatase activities are spatially distinct from each other. Unsteady-state analysis and the sensitivity of the cytoplasmic and cortical PAR-1 models to changes in individual parameters are presented in Figure S5 and Figure S6 and described in Extended Experimental Procedures.

We first considered a model in which PAR-1 activity exists in a linear 5.5-fold gradient in the cytoplasm (low anterior, high posterior). The PAR-1 and phosphatase rates were matched in the posterior to yield slow:fast ratios of 1:1 in the posterior and 2:1 in the anterior, as observed in our FCS measurements (Figure 6B and Table 1). This model gives rise to a temporally stable ~2.9-fold MEX-5 concentration gradient as is observed in vivo. Given a phosphatase rate of 0.1 s^{-1} (within the range reported in the literature of 0.1–100 s^{-1}; Brown and Kholodenko, 1999), the timescale of gradient formation is ~160 s (Figure S5B), consistent with the kinetics observed in vivo (Figure 1). Coordinately changing the absolute kinase and phosphatase rates over two orders of magnitude has little effect on the strength of the gradient. For example, increasing or decreasing both the kinase and phosphatase rates by a factor of 10 generates 3.0- and 2.8-fold MEX-5 gradients, respectively (Figures S5G and S5H). If only the kinase or phosphatase rate is changed (rather than changing them coordinately), the MEX-5 gradient is lost (Figures S5C–S5F). For example, reducing phosphatase activity while maintaining PAR-1 activity increases the proportion of fast-diffusing species and flattens the MEX-5 gradient (Figure 6C and Figure S5D), as observed in *let-92(RNAi)* embryos (Figures 3C and 3D). Interestingly, the MEX-5 concentration gradient is always weaker than the PAR-1 activity gradient (see Discussion).

We next considered a model where PAR-1 is entirely cortical and instantaneously phosphorylates MEX-5. In this cortical-only PAR-1 model, the extent of PAR-1's influence on MEX-5 is determined by the phosphatase rate. For example, at a k_{phos} = 0.1 s^{-1}, the effect on MEX-5 drops off sharply within 10 μm of the cortex (Figure 6D and Figure S6B). A phosphatase rate of k_{phos} = 0.01 s^{-1} would generate an ~3-fold MEX-5 gradient (Figure 6E and Figure S6C). However, nearly all MEX-5 would be in the slow-diffusing state, in contrast to our FCS observations. A gradient with the observed proportions of fast- and slow-diffusing MEX-5 species is only obtained at a phosphatase rate of k_{phos} = 0.0001 s^{-1}. However, the approach to steady state would be ~17 min, far slower than what is observed in vivo (Figure 6K and Figure S6D). Thus, the cortical-only PAR-1 model is not able to simultaneously explain the relative proportions of fast and slow species while also maintaining a rapid approach to steady state. Taken together, the modeling analyses support a critical role for cytoplasmic PAR-1 and demonstrate that the MEX-5 diffusion gradient is sufficient to account for the MEX-5 protein gradient.

DISCUSSION

In this study, we present evidence that the antagonistic activities of PAR-1 and PP2A regulate MEX-5 diffusion to establish the MEX-5 protein gradient. We propose the following model. MEX-5 is in dynamic, local equilibrium between different diffusive RNA complexes in the cytoplasm. Phosphorylation of S404 by PAR-1 biases MEX-5 toward faster-diffusing complexes, and dephosphorylation by PP2A returns MEX-5

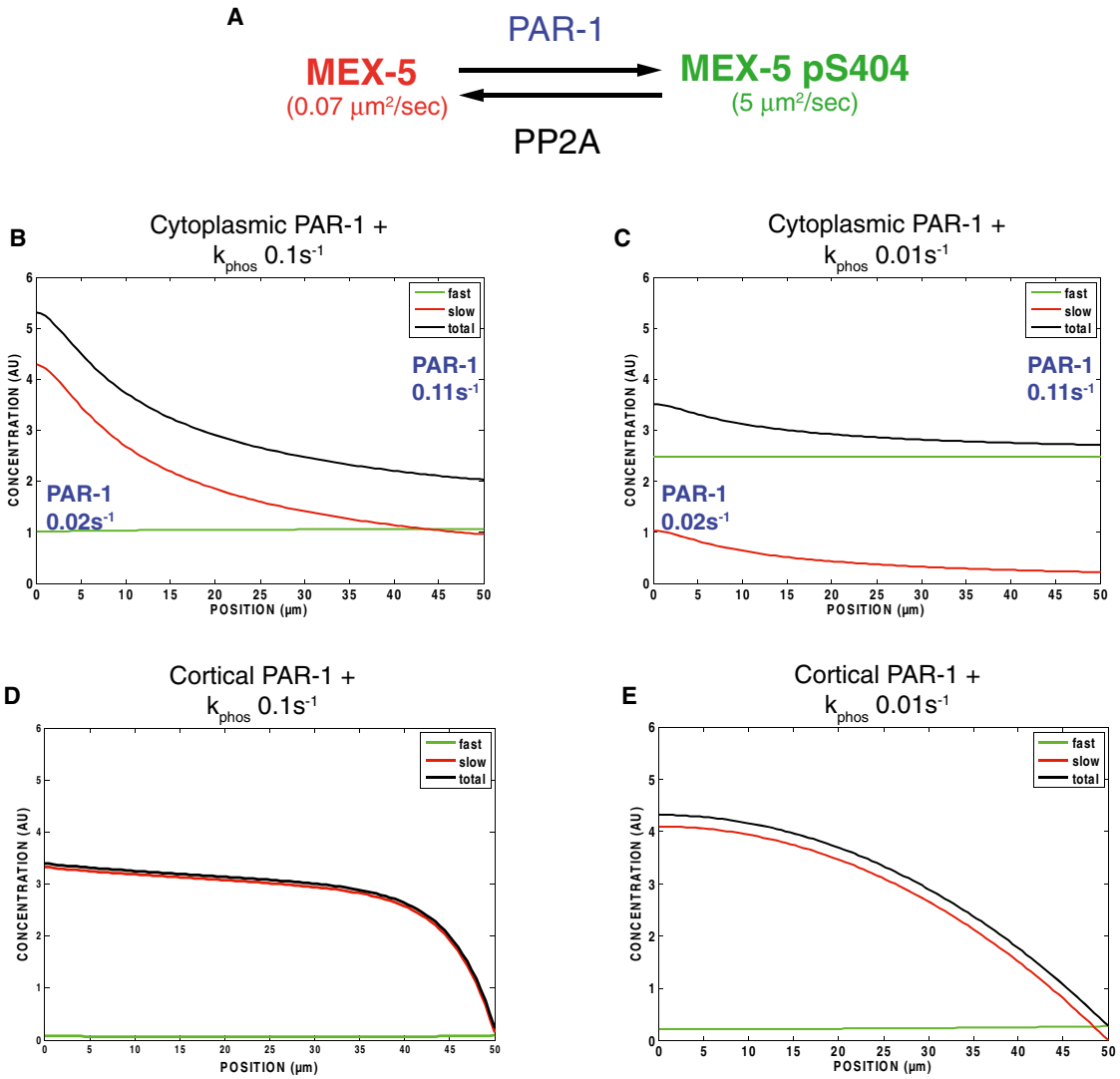

Figure 6. Mathematical Modeling of the MEX-5 Gradient

(A) *Model reactions*. PAR-1 and PP2A are assumed to regulate interconversion between fast and slow MEX-5 species through a phosphorylation cycle. See Table 1 for assumptions used in the model.

(B–E) Graphs showing the model-generated distribution of MEX-5 at steady state along the anterior-posterior axis (anterior end, 0 μm; posterior end, 50 μm). See Extended Experimental Procedures and Figure S5 and Figure S6 for unsteady-state analysis.

(B) *Cytoplasmic PAR-1 model*. PAR-1 activity is assumed to be linearly distributed in the cytoplasm (low in anterior; high in posterior). This imposes an oppositely oriented MEX-5 gradient with the fast and slow species approximately equal in concentration in the posterior and the slow species enriched in the anterior. The total MEX-5 gradient primarily reflects the gradient in slow-diffusing MEX-5. The rapid diffusion of the fast-diffusing species effectively counteracts its asymmetric formation in the posterior. See Figure S5B for unsteady-state analysis.

(C) *PP2A depletion*. Reducing the phosphatase rate by 10-fold weakens the MEX-5 gradient and increases the proportion of phosphorylated MEX-5. See Figure S5D for unsteady-state analysis.

(D) *Posterior cortical PAR-1 plus uniform phosphatase (k_{phos} = 0.1 s^{-1})*. See Figure S6B for unsteady-state analysis.

(E) *Posterior cortical PAR-1 plus uniform phosphatase (k_{phos} = 0.01 s^{-1})*. See Figure S6C for unsteady-state analysis.

into slower-diffusing complexes. Before polarization, PP2A activity dominates over PAR-1, pS404 levels are low, and the majority of MEX-5 molecules are in slow-diffusing complexes. At polarity onset, an unknown mechanism favors PAR-1 activity over PP2A, causing pS404 levels to rise and MEX-5 to enter faster complexes. During polarization, the PP2A/PAR-1 balance is changed along the anterior-posterior axis as PAR-1 becomes enriched in a posterior-to-anterior gradient in the cytoplasm and on the posterior cortex, causing MEX-5 to switch from phosphorylated (on average faster-diffusing) to unphosphorylated (on average slower-diffusing), as it diffuses down the PAR-1 gradient. As a result, MEX-5 redistributes in a gradient opposite PAR-1. We consider each aspect of this model in turn.

Table 1. Parameters and Variables for Cytoplasmic PAR-1 Model

Parameter/Variable	Symbol	Value	Units	Notes
Slow diffusion coefficient	D_{slow}	0.07	$\mu m^2/s$	
Fast diffusion coefficient	D_{fast}	5	$\mu m^2/s$	
Kinase (PAR-1) rate constant	$k_{kin}(x)$	0.02–0.11	s^{-1}	Linear rise along A/P axis
Phosphatase rate constant	k_{phos}	0.1	s^{-1}	Uniform along A/P axis
Embryo length	L	50	μm	

Additional notes:

(1) Kinase and phosphatase rates can be varied coordinately over a range of values (e.g., $k_{kin}(x) = 0.2–1.1\ s^{-1}$ and $k_{phos} = 1\ s^{-1}$ yields similar results). Rate constants must be approximately equal in the posterior region to obtain 1:1 slow:fast diffusing species, and $k_{phos} > k_{kin}$ to obtain >1:1 slow:fast in the anterior region.

(2) Kinase rate constant gradient needs to be larger than the MEX-5 gradient. Here it is assumed that the PAR-1 activity gradient is 5.5-fold, resulting in ~2.9-fold MEX-5 concentration gradient.

(3) Posterior cortical-only PAR-1 case modeled with instantaneous kinase reaction at the right boundary (i.e., x = L), $k_{kin}(x) = 0\ s^{-1}$ and $k_{phos} = 0.1\ s^{-1}$ (Figure 6D) or $k_{phos}=0.01 s^{-1}$ (Figure 6E).

MEX-5 Diffusion Is Retarded by Binding to RNA throughout the Cytoplasm

Our FCS analysis indicates that MEX-5 distributes between two classes of diffusive complexes: a "fast" class averaging 5.15 $\mu m^2/s$ and a "slow" class averaging 0.086 $\mu m^2/s$. Both classes are present throughout the cytoplasm, but the slow class is distributed in an anterior-high to posterior-low gradient. Because FCS analysis only constrains the minimum number of diffusive species, we cannot distinguish whether MEX-5 participates in two or more complexes. The broad range of diffusion coefficients for the fast and slow components and the broad distribution of Dendra::MEX-5 in sucrose gradients suggest, in fact, that MEX-5 may interact with a large range of complexes.

Several lines of evidence suggest that MEX-5's association with slow-diffusive complexes depends on binding to RNA. First, mutations in the CCCH fingers that reduce MEX-5 affinity for RNA increase MEX-5 diffusion and reduce the steepness of the MEX-5 gradient. Second, sucrose gradient fractionation demonstrates that MEX-5 associates with high-density complexes (comparable to 80S ribosomes) in a manner dependent on RNA and the MEX-5 RNA-binding domain. Third, the D_c for the slow species is consistent with mRNP diffusion rates (0.01–0.09 $\mu m^2/s$) in the cytoplasm of *E. coli* and in the nucleus of mammalian cells (Golding and Cox, 2004; Shav-Tal et al., 2004). Because mutations that block MEX-5 phosphorylation (S404A) cause the slow MEX-5 species to be symmetrically distributed even in wild-type zygotes, we do not favor a model wherein MEX-5 diffusion is retarded by binding to a subclass of asymmetrically localized mRNAs. Rather, we suggest that MEX-5 interacts dynamically with many mRNAs throughout the cytoplasm. Consistent with MEX-5 functioning as a broad-spectrum RNA-binding protein, MEX-5 binds to poly-U tracks, which are common in *C. elegans* 3′ untranslated regions (UTRs) (Pagano et al., 2007), and activates maternal mRNA turnover in somatic blastomeres after the two-cell stage (Gallo et al., 2008).

Our mutational analysis also indicates that the amino terminus of MEX-5 contributes to, but is not sufficient for, slow MEX-5 diffusion. This region is rich in polyglutamine stretches, which could mediate MEX-5 self-association. One possibility is that, as proposed for Bruno in *Drosophila*, MEX-5 uses self-interactions and RNA binding to assemble into large ribonucleoprotein particles with retarded diffusion (Chekulaeva et al., 2006).

Phosphorylation of S404 by PAR-1 Biases MEX-5 toward Fast Complexes, and Dephosphorylation by PP2A Returns MEX-5 into Slow Complexes

In the absence of PAR-1, fast and slow MEX-5 complexes are distributed in a 30:70 constant ratio throughout the cytoplasm, indicating that phosphorylation enhances, but is not essential for, the formation of fast MEX-5 complexes. Because conditions predicted to reduce (*par-1(it51)*) or increase (*let-92(RNAi)*) phosphorylation have opposite effects on MEX-5 diffusivity, we suggest that phosphorylation promotes the shifting of MEX-5 from slow- to fast-diffusing complexes. Consistent with this view, MEX-5(S404A) was enriched in the heavier sucrose gradient fractions compared to wild-type MEX-5. In our simulation of the MEX-5 gradient, MEX-5 must switch multiple times between phosphostates as it diffuses across the embryo (see discussion in Extended Experimental Procedures). Consistent with this possibility, we find that pS404 is highly labile in embryo extracts. We suggest that the rapid turnover of pS404 renders MEX-5 exquisitely sensitive to changes in PAR-1 distribution.

Cytoplasmic PAR-1 Is Essential for the Formation of the MEX-5 Gradient

Our simulations also demonstrate the importance of cytoplasmic PAR-1 in specifying the MEX-5 gradient. In the cortical-only PAR-1 model, high k_{phos} values generate MEX-5 gradients that drop off sharply from the posterior cortex, whereas low k_{phos} values yield MEX-5 gradients that form too slowly. In contrast, in the presence of a cytoplasmic PAR-1 activity gradient, a broad range of kinase and phosphatase activities could generate the MEX-5 gradient. Cytoplasmic PAR-1, therefore, eliminates the trade-off between gradient scale and response time. Our in vivo observations confirm that cytoplasmic PAR-1 is sufficient to regulate MEX-5 distribution: most notably, MEX-5 forms a gradient in *par-2(RNAi)* zygotes, which enrich PAR-1 in the posterior cytoplasm but not on the cortex. That PAR-1 can function off the cortex has also been suggested by Boyd et al. (1996), who noted that *par-2* mutant zygotes localize P granules, a function requiring *par-1* activity (Boyd et al., 1996; Cheeks et al., 2004).

One striking aspect of our model is that the amplitude of the MEX-5 gradient will always be smaller than the PAR-1 activity gradient (an ~2.9-fold MEX-5 gradient requires a 5.5-fold PAR-1 activity gradient). GFP::PAR-1 forms an ~3- to 4-fold cytoplasmic concentration gradient, and regulation of PAR-1 kinase activity along the anterior-posterior axis could also contribute to an overall PAR-1 activity gradient. PAR-1 kinase activity has been suggested to be regulated by several mechanisms (Marx et al., 2010), including inhibition by aPKC (Hurov et al., 2004).

aPKC phosphorylates PAR-1 in vitro on a conserved threonine (T983) required for PAR-1 asymmetry in vivo (E.E.G., Y. Hao, and G.S., unpublished data). One possibility is that phosphorylation by anteriorly enriched PKC-3 regulates both PAR-1 activity and levels along the anterior-posterior axis. In polarized T cells, PAR1b/EMK/MARK2 forms a cytoplasmic gradient near the immunological synapse that depends on PKC phosphorylation sites (Lin et al., 2009). These observations raise the possibility that the polarizing effects of the PAR network depend on the formation of cytoplasmic PAR-1 gradients in several cell types.

The "reactive surface" model of Daniels et al. (2010) proposes that MEX-5 diffusion is regulated at the cortex by interactions with both anterior and posterior PARs. Anterior PARs convert phosphorylated MEX-5 into a slower-diffusive form (0.4–1 $\mu m^2/s$), which must be dephosphorylated before conversion back into a faster ($\sim$15 $\mu m^2/s$) form by the posterior PARs (Daniels et al., 2010). The "reactive surface" model does not consider the behavior of the slowest MEX-5 species, which in our FCS analysis account for >50% of total MEX-5 (average 0.086 $\mu m^2/s$, range 0.025 to 0.16 $\mu m^2/s$). Furthermore, this model predicts that loss of phosphatase activity should slow MEX-5 diffusion, whereas we find that loss of the PP2A phosphatase increases MEX-5 diffusivity. This model also predicts that, under conditions where MEX-5 is phosphorylated (PAR-1 active), loss of anterior PARs should increase MEX-5 diffusivity. In contrast, we find that *pkc-3(RNAi)* has no effect on MEX-5 diffusivity in *par-1(b274)* zygotes (Figure 2C). Our genetic analyses demonstrate that *par-1* is fully epistatic to *pkc-3* with respect to MEX-5 diffusivity, making a direct contribution by anterior PARs unlikely. Rather, our data indicate that anterior PARs regulate MEX-5 diffusion indirectly, by controlling the distribution (and possibly the activity) of PAR-1 along the anterior-posterior axis.

Formation of Concentration Gradients by Spatially Segregated Modification Enzymes

The model of Lipkow and Odde (2008) can be used to form gradients at any cellular scale by varying diffusion and phosphatase rates. The MEX-5 gradient is established in an $\sim$50 μm zygote, but the same principles could account for the apparent CheY gradient that emerges in the cytoplasm of *E. coli* ($\sim$5 μm) upon uncoupling of the phosphatase/kinase pair CheZ/CheA (Vaknin and Berg, 2004). Spatial segregation of kinase and phosphatase activities has been shown to lead to phosphogradients in many cell types from bacteria to eukaryotic cells (Brown and Kholodenko, 1999; Coppey et al., 2008; Fuller et al., 2008; Kalab et al., 2002; Maeder et al., 2007; Su et al., 1998). Our modeling analyses demonstrate that a spatially biased kinase and phosphatase cycle can give rise to protein concentration gradients even under conditions where the phosphogradient is weak. Despite higher PAR-1 activity in the posterior, phosphorylated MEX-5 is predicted to distribute almost evenly across the zygote due to its faster diffusion (Figure 6). In principle, any posttranslational modification cycle could generate a protein concentration gradient, as long as the opposing enzymes are spatially segregated and the modification affects protein diffusion rates. We suggest that the mechanism we uncover here for MEX-5 can be applied broadly to understanding rapid changes in the distribution of cytoplasmic proteins in a variety of cell types.

EXPERIMENTAL PROCEDURES

Detailed experimental procedures are described in the Extended Experimental Procedures.

C. elegans Strains

Transgenic worms used in this study are listed in Table S1.

Determination of Dendra^R::MEX-5 Diffusion Coefficients

Dendra::MEX-5 was photoconverted in a stripe with UV light and imaged on a spinning disk confocal microscope. Intensity values were fit to Gaussian distributions for each time point (GraphPad Prism), and the change in variance over time was used to calculate D_c (Berg, 1993).

Recombinant Protein Purification, Kinase Assays, and Dephosphorylation Assays

MBP:MEX-5 and MBP:PAR-1 (1–492, T325E) were partially purified from *E. coli* and incubated at 30°C in the presence of [^{32}P]-ATP or cold ATP. For nonisotopic phosphorylation and dephosphorylation assays, kinase reactions were terminated with 20 nM staurosporine before embryonic extract was added.

Immunoprecipitations

MEX-5 pS404 phosphospecific antibodies coupled to ProteinG dynabeads were used to immunoprecipitate from whole worm extracts.

Sucrose Gradient Fractionation

Cycloheximide-treated whole worm extracts were fractionated over 10%–45% linear sucrose gradients at 39,000 rpm for 3 hr. Fractions were collected after passing the gradient through a UV detector, and the distribution of Dendra::MEX-5 was determined by western blot with anti-Dendra antibodies (Axxora).

Fluorescence Correlation Spectroscopy

GFP::MEX-5 levels were reduced by partial GFP RNAi depletion prior to imaging. Embryos were imaged on a Zeiss LSM 510 Confocal microscope equipped with a Confocor 3 FCS. Autocorrelation curves were analyzed within the Zeiss Confocor 3 software package.

Modeling of the MEX-5 Gradient

Parameters used in the models are listed in Table 1. A detailed description of model and the contribution of individual parameters to the steady-state and unsteady-state models are provided in the Extended Experimental Procedures.

SUPPLEMENTAL INFORMATION

Supplemental Information includes Extended Experimental Procedures, six figures, and one table and can be found with this article online at doi:10.1016/j.cell.2011.08.012.

ACKNOWLEDGMENTS

We thank F. Motegi for providing the Dendra2 construct, S. He for help with sucrose gradients, and N. Perkins and E. Pryce at the JHU Integrated Imaging Center for assistance with FCS. We thank K. Kemphues for providing strains and antibodies. We thank A. Cuenca for generation of the GFP::PAR-1 transgenic strain. We thank S. Kuo for helpful conversations and members of the Seydoux lab for helpful comments on the manuscript. This work was supported by the National Institutes of Health (Grants R01HD37047 [G.S.] and R01 GM71522 [D.J.O.]) and the American Cancer Society (Grant PF-08-158-01-DDC [E.E.G.]). G.S. is an Investigator of the Howard Hughes Medical Institute.

Received: March 3, 2011
Revised: June 17, 2011
Accepted: August 8, 2011
Published: September 15, 2011

REFERENCES

Berg, H.C. (1993). Random Walks in Biology, Expanded Edition edn (Princeton, New Jersey: Princeton University Press).

Boyd, L., Guo, S., Levitan, D., Stinchcomb, D.T., and Kemphues, K.J. (1996). PAR-2 is asymmetrically distributed and promotes association of P granules and PAR-1 with the cortex in C. elegans embryos. Development *122*, 3075–3084.

Brown, G.C., and Kholodenko, B.N. (1999). Spatial gradients of cellular phospho-proteins. FEBS Lett. *457*, 452–454.

Budirahardja, Y., and Gönczy, P. (2008). PLK-1 asymmetry contributes to asynchronous cell division of C. elegans embryos. Development *135*, 1303–1313.

Cheeks, R.J., Canman, J.C., Gabriel, W.N., Meyer, N., Strome, S., and Goldstein, B. (2004). C. elegans PAR proteins function by mobilizing and stabilizing asymmetrically localized protein complexes. Curr. Biol. *14*, 851–862.

Chekulaeva, M., Hentze, M.W., and Ephrussi, A. (2006). Bruno acts as a dual repressor of oskar translation, promoting mRNA oligomerization and formation of silencing particles. Cell *124*, 521–533.

Coppey, M., Boettiger, A.N., Berezhkovskii, A.M., and Shvartsman, S.Y. (2008). Nuclear trapping shapes the terminal gradient in the Drosophila embryo. Curr. Biol. *18*, 915–919.

Cuenca, A.A., Schetter, A., Aceto, D., Kemphues, K., and Seydoux, G. (2003). Polarization of the C. elegans zygote proceeds via distinct establishment and maintenance phases. Development *130*, 1255–1265.

Daniels, B.R., Dobrowsky, T.M., Perkins, E.M., Sun, S.X., and Wirtz, D. (2010). MEX-5 enrichment in the C. elegans early embryo mediated by differential diffusion. Development *137*, 2579–2585.

Ephrussi, A., and St Johnston, D. (2004). Seeing is believing: the bicoid morphogen gradient matures. Cell *116*, 143–152.

Fuller, B.G., Lampson, M.A., Foley, E.A., Rosasco-Nitcher, S., Le, K.V., Tobelmann, P., Brautigan, D.L., Stukenberg, P.T., and Kapoor, T.M. (2008). Midzone activation of aurora B in anaphase produces an intracellular phosphorylation gradient. Nature *453*, 1132–1136.

Gallo, C.M., Munro, E., Rasoloson, D., Merritt, C., and Seydoux, G. (2008). Processing bodies and germ granules are distinct RNA granules that interact in C. elegans embryos. Dev. Biol. *323*, 76–87.

Golding, I., and Cox, E.C. (2004). RNA dynamics in live Escherichia coli cells. Proc. Natl. Acad. Sci. USA *101*, 11310–11315.

Goldstein, B., and Macara, I.G. (2007). The PAR proteins: fundamental players in animal cell polarization. Dev. Cell *13*, 609–622.

Guo, S., and Kemphues, K.J. (1995). par-1, a gene required for establishing polarity in C. elegans embryos, encodes a putative Ser/Thr kinase that is asymmetrically distributed. Cell *81*, 611–620.

Gurskaya, N.G., Verkhusha, V.V., Shcheglov, A.S., Staroverov, D.B., Chepurnykh, T.V., Fradkov, A.F., Lukyanov, S., and Lukyanov, K.A. (2006). Engineering of a monomeric green-to-red photoactivatable fluorescent protein induced by blue light. Nat. Biotechnol. *24*, 461–465.

Hudson, B.P., Martinez-Yamout, M.A., Dyson, H.J., and Wright, P.E. (2004). Recognition of the mRNA AU-rich element by the zinc finger domain of TIS11d. Nat. Struct. Mol. Biol. *11*, 257–264.

Hurd, D.D., and Kemphues, K.J. (2003). PAR-1 is required for morphogenesis of the Caenorhabditis elegans vulva. Dev. Biol. *253*, 54–65.

Hurov, J.B., Watkins, J.L., and Piwnica-Worms, H. (2004). Atypical PKC phosphorylates PAR-1 kinases to regulate localization and activity. Curr. Biol. *14*, 736–741.

Kalab, P., Weis, K., and Heald, R. (2002). Visualization of a Ran-GTP gradient in interphase and mitotic Xenopus egg extracts. Science *295*, 2452–2456.

Kao, G., Tuck, S., Baillie, D., and Sundaram, M.V. (2004). C. elegans SUR-6/PR55 cooperates with LET-92/protein phosphatase 2A and promotes Raf activity independently of inhibitory Akt phosphorylation sites. Development *131*, 755–765.

Kemphues, K. (2000). PARsing embryonic polarity. Cell *101*, 345–348.

Krahn, M.P., Egger-Adam, D., and Wodarz, A. (2009). PP2A antagonizes phosphorylation of Bazooka by PAR-1 to control apical-basal polarity in dividing embryonic neuroblasts. Dev. Cell *16*, 901–908.

Lai, W.S., Kennington, E.A., and Blackshear, P.J. (2002). Interactions of CCCH zinc finger proteins with mRNA: non-binding tristetraprolin mutants exert an inhibitory effect on degradation of AU-rich element-containing mRNAs. J. Biol. Chem. *277*, 9606–9613.

Lin, J., Hou, K.K., Piwnica-Worms, H., and Shaw, A.S. (2009). The polarity protein Par1b/EMK/MARK2 regulates T cell receptor-induced microtubule-organizing center polarization. J. Immunol. *183*, 1215–1221.

Lipkow, K., and Odde, D.J. (2008). Model for protein concentration gradients in the cytoplasm. Cell. Mol. Bioeng. *1*, 84–92.

Lippincott-Schwartz, J., and Patterson, G.H. (2008). Fluorescent proteins for photoactivation experiments. Methods Cell Biol. *85*, 45–61.

Little, S.C., Tkačik, G., Kneeland, T.B., Wieschaus, E.F., and Gregor, T. (2011). The formation of the Bicoid morphogen gradient requires protein movement from anteriorly localized mRNA. PLoS Biol. *9*, e1000596.

Lizcano, J.M., Göransson, O., Toth, R., Deak, M., Morrice, N.A., Boudeau, J., Hawley, S.A., Udd, L., Mäkelä, T.P., Hardie, D.G., and Alessi, D.R. (2004). LKB1 is a master kinase that activates 13 kinases of the AMPK subfamily, including MARK/PAR-1. EMBO J. *23*, 833–843.

Maeder, C.I., Hink, M.A., Kinkhabwala, A., Mayr, R., Bastiaens, P.I., and Knop, M. (2007). Spatial regulation of Fus3 MAP kinase activity through a reaction-diffusion mechanism in yeast pheromone signalling. Nat. Cell Biol. *9*, 1319–1326.

Marx, A., Nugoor, C., Panneerselvam, S., and Mandelkow, E. (2010). Structure and function of polarity-inducing kinase family MARK/Par-1 within the branch of AMPK/Snf1-related kinases. FASEB J. *24*, 1637–1648.

Mello, C.C., Schubert, C., Draper, B., Zhang, W., Lobel, R., and Priess, J.R. (1996). The PIE-1 protein and germline specification in C. elegans embryos. Nature *382*, 710–712.

Moravcevic, K., Mendrola, J.M., Schmitz, K.R., Wang, Y.H., Slochower, D., Janmey, P.A., and Lemmon, M.A. (2010). Kinase associated-1 domains drive MARK/PAR1 kinases to membrane targets by binding acidic phospholipids. Cell *143*, 966–977.

Nam, S.C., Mukhopadhyay, B., and Choi, K.W. (2007). Antagonistic functions of Par-1 kinase and protein phosphatase 2A are required for localization of Bazooka and photoreceptor morphogenesis in Drosophila. Dev. Biol. *306*, 624–635.

Pagano, J.M., Farley, B.M., McCoig, L.M., and Ryder, S.P. (2007). Molecular basis of RNA recognition by the embryonic polarity determinant MEX-5. J. Biol. Chem. *282*, 8883–8894.

Rivers, D.M., Moreno, S., Abraham, M., and Ahringer, J. (2008). PAR proteins direct asymmetry of the cell cycle regulators Polo-like kinase and Cdc25. J. Cell Biol. *180*, 877–885.

Schlaitz, A.L., Srayko, M., Dammermann, A., Quintin, S., Wielsch, N., MacLeod, I., de Robillard, Q., Zinke, A., Yates, J.R., 3rd, Müller-Reichert, T., et al. (2007). The C. elegans RSA complex localizes protein phosphatase 2A to centrosomes and regulates mitotic spindle assembly. Cell *128*, 115–127.

Schubert, C.M., Lin, R., de Vries, C.J., Plasterk, R.H., and Priess, J.R. (2000). MEX-5 and MEX-6 function to establish soma/germline asymmetry in early C. elegans embryos. Mol. Cell *5*, 671–682.

Severson, A.F., and Bowerman, B. (2003). Myosin and the PAR proteins polarize microfilament-dependent forces that shape and position mitotic spindles in Caenorhabditis elegans. J. Cell Biol. *161*, 21–26.

Shav-Tal, Y., Darzacq, X., Shenoy, S.M., Fusco, D., Janicki, S.M., Spector, D.L., and Singer, R.H. (2004). Dynamics of single mRNPs in nuclei of living cells. Science *304*, 1797–1800.

St Johnston, D., and Ahringer, J. (2010). Cell polarity in eggs and epithelia: parallels and diversity. Cell *141*, 757–774.

Su, T.T., Sprenger, F., DiGregorio, P.J., Campbell, S.D., and O'Farrell, P.H. (1998). Exit from mitosis in Drosophila syncytial embryos requires proteolysis and cyclin degradation, and is associated with localized dephosphorylation. Genes Dev. *12*, 1495–1503.

Tenlen, J.R., Molk, J.N., London, N., Page, B.D., and Priess, J.R. (2008). MEX-5 asymmetry in one-cell C. elegans embryos requires PAR-4- and PAR-1-dependent phosphorylation. Development *135*, 3665–3675.

Vaknin, A., and Berg, H.C. (2004). Single-cell FRET imaging of phosphatase activity in the Escherichia coli chemotaxis system. Proc. Natl. Acad. Sci. USA *101*, 17072–17077.

Wartlick, O., Kicheva, A., and González-Gaitán, M. (2009). Morphogen gradient formation. Cold Spring Harb. Perspect. Biol. *1*, a001255.

Yoder, J.H., Chong, H., Guan, K.L., and Han, M. (2004). Modulation of KSR activity in Caenorhabditis elegans by Zn ions, PAR-1 kinase and PP2A phosphatase. EMBO J. *23*, 111–119.

EXTENDED EXPERIMENTAL PROCEDURES

Transgenics and Worm Strains

Dendra::MEX-5 constructs were constructed as follows. A 4.4 kb *mex-5* promoter fragment based on Tenlen et al. (2008) was cloned into pDONRP4P1R (Invitrogen). Dendra2/TEV/S-peptide (Gallo et al., 2010) was cloned into pDONR201. A MEX-5 genomic fragment from the start ATG through 648 bp of 3′UTR was cloned into pDONRP2RP3. Exon 2 of *mex-5* was recoded to be RNAi-resistant (GenScript) so as to allow depletion of endogenous MEX-5/6 without depletion of the transgene. These constructs were assembled into pCG150 using three-way Gateway system (LR reaction) (Invitrogen) (Merritt et al., 2008). Mutations were made by recombinant PCR and all inserts were sequenced verified. The wild-type Dendra::MEX-5 transgene rescued *mex-5(RNAi)* to 97% viability (n = 244) and *mex-5/6(RNAi)* to 58% viability (n = 136). GFP::MEX-5 transgenes were constructed in the same way as Dendra::MEX-5 constructs except a pDONR201-GFP/TEV/FLAG entry clone was used and wild-type sequence of MEX-5 exon 2 was used. MEX-5 transgenes driven by the *pie-1* promoter and *pie-1* 3′UTR were constructed by cloning the *mex-5* cDNA as a SpeI fragment downstream of a Dendra2/TEV/S-peptide tag cloned into pIC26 LAP tag (Cheeseman et al., 2004). GFP::PAR-1 was constructed by cloning PAR-1 cDNA into pDONR201 and then recombining into pID3.01, a Gateway destination vector containing the *pie-1* promoter, GFP, and *pie-1* 3′UTR. The GFP::PAR-1 transgene rescues the embryonic lethality of *par-1(it32)*: GFP::PAR-1; *par-1(it32)* hermaphrodites are self-fertile and can be maintained over several generations. GFP::PAR-1 localization patterns were the same in wild-type and *par-1(it32)* backgrounds. Transgenic lines were generated by microparticle bombardment (Praitis et al., 2001) and are listed in Table S1. The following mutant strains were used in this study: *par-1(it51) rol-4(sc8)/DnT1*, *par-1(b274) rol-4(sc8)/DnT1* (Guo and Kemphues, 1995), *mex-6(pk440); mex-5(zu199) unc-30(e191)/nT1* (Schubert et al., 2000). To identify the mutation in *par-1(b274),* PAR-1 exons were PCR amplified and sequenced as PCR products from wild-type, *par-1 (it51)*, and *par-1(b274)* homozygous worms.

Live Microscopy

Embryos were dissected in egg salts on a coverslip and inverted onto a 3% agarose pad. Spinning disk confocal images were collected on a Zeiss Axio Imager.Z1 microscope with a 63× 1.4 NA oil immersion objective and collected on a QuantEM 512SC camera (Photometrics). The microscope was controlled by the Slidebook software package (Intelligent Imaging Innovations, Inc.). Fluorescence intensities were determined from a single midplane images (the plane in which the pronuclei are in focus) and corrected for background by subtracting signal outside the embryo (Image J). Anterior/posterior concentration ratios were determined by dividing the average fluorescence intensity in the anterior cytoplasm by the average fluorescence intensity in the posterior cytoplasm (anterior/posterior boundary was defined as 50% embryo length). GFP::PAR-1 quantification was also corrected for embryo autofluorescence (which fluoresces in the same channel as GFP) by subtracting signal averaged from eight wild-type nontransgenic zygotes.

Antibodies and Immunofluorescence

For immunofluorescence, gravid hermaphrodites were dissected in M9 media on 0.1% Poly-L-lysine-coated slides, placed under a coverslip, frozen on dry ice-chilled aluminum blocks, and freeze-cracked by removing the coverslips. For PAR-1 and PKC-3 staining, slides were incubated in −20°C methanol for 15 min, −20°C acetone for 10 min, and blocked in PBT + 0.1% BSA for 30 min. For MEX-5 staining, slides were fixed in −20°C methanol for 2 min and 2% paraformaldehyde for 20 min at 24°C, then blocked in PBT + 0.1% BSA for 30 min. Antibody dilutions were as follows: 1:100 rat anti-PKC-3 (Aono et al., 2004), 1:50 rabbit anti-PAR-1 (Guo and Kemphues, 1995), 1:100 guinea pig anti-MEX-5 (this study). For western blotting, anti-PAR-1 antibody (Guo and Kemphues, 1995) was diluted 1:1000 and anti-MEX-5 antibody was diluted 1:500.

Anti-MEX-5 antibodies were raised in two guinea pigs immunized with the peptide RMSHDDQDYDQDVIPEDYKKKC (Covance). Phosphospecific antibodies were generated by Bethyl laboratories in rabbits using the peptides RNVAG(pS)MMCLSN (MEX-5 pS404) and CSTKWT(pS)EENLG (MEX-5 pS458).

Determination of Dendra^{R}::MEX-5 Diffusion Coefficients

Dendra::MEX-5 was photoconverted using either an 800 ms pulse of 405 nm laser controlled by a Mosaic Digital Illumination System (Photonic Instruments, INC) or a 3 s pulse of light from a EXFO X-cite120 metal halide epifluorescence light source passed through a thin slit in a single layer of aluminum foil placed in front of a DAPI filter cube. Two exposures prior and fifteen exposures following photoconversion were collected (every 1.05 or 1.8 s). For all experiments except Figure 1D and Figure 1E "short axis," Dendra::MEX-5 was photoactivated in a stripe along the long axis positioned at the middle of the cell. For Figure 1E "short axis," Dendra::MEX-5 was photoactivated at ~50% embryo length in a line perpendicular to the anterior/posterior axis. Time-lapse images were analyzed in ImageJ (NIH). For Figure 1E intensity was averaged at the indicated positions in a 10 by 120 pixel box drawn perpendicular to the photoactivation stripe. For all other figures, intensity was averaged in a 20 by 120 pixel box positioned perpendicular to the photoactivation stripe at 25% and 75% embryo length. Intensity values were fit to Gaussian distributions for each time point (GraphPad Prism). The standard deviation of the Gaussian was converted to variance in microns and plotted versus time. The slope of the linear regression = $2D_c$ (Berg, 1993). Error bars are standard error of the mean from a minimum of 5 embryos. For Figure 1E, values along the long axis were derived from 14 embryos before pronuclear formation, 12 embryos at pronuclear formation, and 5 embryos at

embryos at NEBD. Values along the short axis were derived from 4 embryos before pronuclear formation, 11 embryos at pronuclear formation and 11 embryos at NEBD. For all other figures, apparent diffusion coefficients were derived from at least 5 embryos.

RNAi and Latrunculin A Treatment

RNAi was induced by feeding worms bacteria expressing double-stranded RNA as in (Timmons and Fire, 1998). For PAR-1 depletion prior to immunoprecipitation, worms were synchronized as L1s and then plated as L4s on bacteria expressing double-stranded PAR-1 RNA for 28 hr at 25°C. Latrunculin A (Sigma) treatment was performed as in Severson and Bowerman (2003), except that worms were fed *F08F8.2(RNAi)* bacteria for 24 hr at 25°C to increase egg shell permeability (Redemann et al., 2010).

Recombinant Protein Expression

Gateway cloning was used to clone full-length MEX-5 and PAR-1(1-492) PCR products into pDONR201 (Invitrogen). pDONR constructs were recombined into the destination vector pJP1.09 (Stitzel et al., 2006). MBP-fusion proteins were expressed in *E. coli* strain CAG-456 overnight at 16°C following induction with 400 μM isopropyl-β-D-1-thiogalactopyranoside (IPTG). MBP:MEX-5 cultures were supplemented with 0.1 mM $ZnCl_2$ at the time of induction. Bacterial pellets were sonicated in cold column buffer (20 mM Tris 7.4, 500 mM NaCl, 0.1 mM $ZnCl_2$, 10% glycerol, 1 mM DTT for MBP:MEX-5, and 20 mM Tris 7.4, 500 mM NaCl, 1 mM EDTA, 10% glycerol, 1 mM DTT for MBP:PAR-1(aa 1492, T325E)) and centrifuged for 30 min at ~20,000 g. Lysate supernatants were bound in batch to amylose resin (New England Biolabs), washed extensively and eluted with column buffer containing 10 mM maltose. Partially purified proteins were aliquoted and stored at −80°C.

Kinase and Dephosphorylation Assays

Isotopic kinase assays were performed by incubating MBP:MEX-5 with MBP:PAR-1(aa 1–492, T325E) in 20 mM Tris (7.4),150 mM NaCl, 10 μM ATP, and 2.5 μCi [^{32}P] ATP (NEN) for 30 min at 30°C. Reactions were terminated by addition of NuPAGE LDS sample buffer (Invitrogen) and heating for 10 min at 70°C. For cold kinase and dephosphorylation assays, MBP:MEX-5 was incubated in 20 mM Tris (7.4),150 mM NaCl, 100 μM ATP with MBP:PAR-1(aa 1–492, T325E) at 30°C and samples were taken at the indicated time points. The kinase reaction was terminated after 120 min with 20 nM staurosporine (Sigma). Dephosphorylation assays began with the addition of 0.25 μl embryonic extract with or without pretreatment with 200 nM okadaic acid. Each sample was run on two separate SDS-PAGE gels and processed for western blot using pS404 and pS458 antibodies. Embryonic extracts were prepared from embryos sonicated in equal volume 20 mM Tris (7.4), 150 mM NaCl, and 0.05% NP-40 supplemented with Complete protease inhibitors (Roche) and stored in small aliquots at −80°C.

Sucrose Gradient Fractionation

Sucrose gradient fractionation was adapted from Hundley et al. (2008). Young adults (grown from synchronized L1s at 25°C on NEP plates seeded with NA22 bacteria) were washed three times in M9 and two times in lysis buffer (20 mM HEPES (pH 7.4), 5 mM $MgCl_2$, 10 mM KCl, 1 mM $ZnCl_2$, 1 mM EGTA, 10% glycerol). Worms were then incubated for 5 min in 3 volumes of lysis buffer supplemented with 0.5 mg/mL cycloheximide, 0.2 mg/ml heparin, Complete protease inhibitors (Roche), and PhosStop phosphatase inhibitors (Roche) for 5 min and frozen in liquid nitrogen. Worms were ground with a mortar and pestle chilled with liquid nitrogen and stored at −80°C. 1 g of worm powder was lysed in 1 ml Lysis buffer supplemented with protease and phosphatase inhibitors, 0.5 mM DTT, 0.2 mg/ml Heparin, 80 U/ml RNaseOut (Invitrogen), and 0.5 mg/ml cycloheximide by sonication. Lysates were clarified by centrifugation at 4°C for 10 min at 22,000 g. Two hundred microliters of lysate was fractionated on a 10.5 ml linear 10%–45% sucrose gradients (poured with a BioComp Gradient Master in 14 × 89 mm polyallomar tubes (Beckmann #331372)) by centrifugation at 39,000 rpm for 3 hr in a SW41 rotor. Gradients were passed through a UV detector (ISCO UA-6 UV) by pumping Fluorinert FC-40 (Sigma) below the gradients and 700 μl fractions were collected. 30 μl were analyzed by western blot using anti-Dendra antibody diluted 1:10,000 (Axxora).

Immunoprecipitations

Lysates were prepared as for sucrose fractionation except lysis buffer was 20 mM HEPES 7.4, 150 mM NaCl, 5 mM $MgCl_2$, 1 mM $ZnCl_2$, 1 mM EGTA, 0.5 mM DTT, 0.05% NP-40. pS404 antibody was coupled to ProteinG Dynabeads and used to immunoprecipitate from 1 ml of adult worm lysate 4°C overnight, washed four times with 1 ml lysis buffer, and eluted in NuPAGE LDS sample buffer (Invitrogen) for 10 min at 70°C.

Fluorescence Correlation Spectroscopy

Prior to imaging, GFP::MEX-5 expression was reduced by treating at least 50 worms with a dilution series of GFP(RNAi) bacteria diluted from 1:10 to 1:200 in L4440 (empty vector) RNAi bacteria. Worms expressing optimal levels of GFP were indentified empirically each day. Embryos were dissected in egg salts on a coverslip, inverted into a Fluoro-dish culture dish (World Precision Instruments), and immersed in egg salts. Imaging was performed on a Zeiss LSM 510 Confocal microscope equipped with a Confocor 3 FCS module using a 40× water immersion objective. Ten 10 s scans were collected at both 30% and 70% embryo length in the same embryo. The first scan at each position was discarded to avoid photo-bleaching artifacts. Autocorrelation curves were analyzed between time-lags 7.2 μs and 3.35 s using one, two or three component three-dimensional models within the Zeiss Confocor 3

software package. The slow-diffusing species accounts for more than 35% of total MEX-5 when our data are fit to a three-component model using the parameters used in Daniels et al. (2010).

Mathematical Modeling of the MEX-5 Gradient

The model is similar to that described in Lipkow and Odde (2008), with the following modifications. We assume that the kinase is distributed in a linearly increasing concentration along the AP-axis starting at the left boundary of a rectangular cell at x = 0 (i.e., the anterior end of the embryo), and the phosphatase is distributed uniformly throughout the cytoplasm over 0 < x < L. In this case where the kinase acts in the cytoplasm, the governing equations are given by

$$\frac{\partial c_A}{\partial t} = D_A \frac{\partial^2 c_A}{\partial x^2} + k_{phos} c_B - k_{kin}(x) c_A \tag{1}$$

for the dephosphorylated, slow-diffusing form of MEX-5 (here designated as "A") and

$$\frac{\partial c_B}{\partial t} = D_B \frac{\partial^2 c_B}{\partial x^2} - k_{phos} c_B + k_{kin}(x) c_A \tag{2}$$

for the phosphorylated, fast-diffusing form of MEX-5 (here designated as "B"), where D_A and D_B are the diffusion coefficients of A and B, respectively, c_A and c_B are the molar concentrations of A and B, respectively, and k_{phos} and $k_{kin}(x)$ are the first-order phosphatase and kinase rate constants, respectively. At steady-state, these equations become

$$0 = D_A \frac{\partial^2 c_A}{\partial x^2} + k_{phos} c_B - k_{kin}(x) c_A \tag{3}$$

and

$$0 = D_B \frac{\partial^2 c_B}{\partial x^2} - k_{phos} c_B + k_{kin}(x) c_A . \tag{4}$$

The kinase activity gradient in the cytoplasm is assumed to be a linear function of position in the embryo given by

$$k_{kin}(x) = b + mx \tag{5}$$

where m (units: $\mu m^{-1}\, s^{-1}$) and b (units: s^{-1}) are the slope and intercept of the linear gradient. For the cytoplasmic PAR-1 only model (i.e., the base model), no flux boundary conditions were imposed for both A and B at both x = 0 and x = L, so that

$$\left.\frac{\partial c_A}{\partial x}\right|_{x=0} = \left.\frac{\partial c_B}{\partial x}\right|_{x=0} = \left.\frac{\partial c_A}{\partial x}\right|_{x=L} = \left.\frac{\partial c_B}{\partial x}\right|_{x=L} = 0. \tag{6}$$

In the case of PAR-1 acting at the posterior cortex, we modified the boundary conditions at x = L such that

$$-D_A \left.\frac{\partial c_A}{\partial x}\right|_{x=L} = k_{kin,boundary} c_A(L) \tag{7}$$

and

$$-D_B \left.\frac{\partial c_B}{\partial x}\right|_{x=L} = -k_{kin,boundary} c_A(L) \tag{8}$$

where $k_{kin,boundary}$ is the first-order rate constant for the heterogeneous kinase reaction at the right boundary at x = L (set to 3 μm/s, sufficiently high to enforce $c_A(L) \approx 0$). In addition, for the cortical kinase model, $k_{kin}(x) = 0$. At any point in the system, the total protein concentration, $c_T(x)$, is given by

$$c_T(x) = c_A(x) + c_B(x). \tag{9}$$

The initial condition was assumed to be uniformly 70% A (slow) and 30% B (fast), with a total uniform concentration (arbitrary) of 3 μM.

The steady-state governing equations can be recast into a dimensionless form

$$0 = \alpha_A Y_A'' + Y_B - \beta(X) Y_A \tag{10}$$

and

$$0 = \alpha_B Y_B'' - Y_B + \beta(X) Y_A \tag{11}$$

where $Y_A = c_A/c_{T0}$, $Y_B = c_B/c_{T0}$, X = x/L, and

$$\alpha_A = \frac{D_A}{k_{phos}L^2} \tag{12}$$

$$\alpha_B = \frac{D_B}{k_{phos}L^2} \tag{13}$$

$$\beta(X) = \frac{b + mx}{k_{phos}} = \frac{b + mXL}{k_{phos}}. \tag{14}$$

These dimensionless parameters help define regimes in which the cytoplasmic gradient model will work. First, for the cytoplasmic model to yield an appreciable gradient, the slow species must be much slower than the fast species, i.e., $\alpha_B >> \alpha_A$.

In this case, the relatively rapid diffusion of B means that gradients of B will be relatively weak, i.e., that $Y_B \approx$ constant. Thus, the two differential equations become a single equation, given by the following equation, subject to the mass conservation constraint:

$$\int_0^1 (Y_A + Y_B)dX = 1. \tag{15}$$

For the gradient of the slow species of A to be appreciable, the dimensionless parameter α_A must be small, i.e., $\alpha_A << 1$.

As α_A approaches unity, the gradient becomes weaker. Using the base parameter set, we obtain $\alpha_A = 2.8 \times 10^{-4}$, well below unity as required (see section ''Parameter Sensitivity Analysis'' within the Extended Experimental Procedures). In some contexts, such as chemical reaction engineering and in previous modeling of intracellular signaling gradients, this dimensionless parameter is referred to as a Thiele modulus (Froment and Bischoff, 1990; Meyers et al., 2006). The Thiele modulus is a dimensionless number that scales the relative rates of reaction and diffusion given by

$$\Phi_A = \frac{1}{\sqrt{\alpha_A}}. \tag{16}$$

When the Thiele modulus is less than unity (or equivalently when α_A is greater than unity), then the gradient is weak.

The dimensionless quantity, β, gives the relative rate of the kinase and phosphatase rates. Because β depends on position, it is really a variable rather than a parameter. However, it is useful to consider its value at the boundaries, i.e., at X = 0 and at X = 1. Experimentally, $\beta(1)$ is constrained to be $\sim$1 so that the fast and slow species are at about equal concentrations in the posterior cortical region, while $\beta(0) < \beta(1)$ so that the kinase rate increases with X along the AP axis. For our base parameter set, $\beta(1) = 1.1$ and $\beta(0) = 0.2$, and their ratio is $\gamma = \beta(1)/\beta(0) = 5.5$, where γ is a dimensionless parameter that quantifies the steepness of the kinase gradient. When $\gamma = 1$, then there is no gradient in kinase activity; increasing values of γ reflect the increasing steepness of the kinase gradient in the cytoplasm. Additional discussion of the model, including the parametric determinants of the rate of approach to steady-state are included in the following section of the Extended Experimental Procedures.

Steady-State Gradient and Unsteady-State Dynamics of MEX-5 Protein Concentration Gradient Models

Note: In this discussion, the fast-diffusing form of MEX-5 is designated ''A'' and the slow-diffusing form is designated ''B.''

Time and Length Scales of the Model

Using the base set of parameters, we can define a number of dimensional quantities that describe the relationships between space and time in the model. First, molecules in the slow state will diffuse slowly until phosphorylated by the kinase. In the cytoplasmic model, the rate of phosphorylation varies with the position in the cell. At the extreme ends of the cell (X = 0 anterior-most position, X = 1 posterior-most position), the mean time spent in the slow state is given by:

$$\tau_{slow}(X = 0) = \frac{1}{k_{kin}(0)} = \frac{1}{(0.02s^{-1})} = 50s$$

$$\tau_{slow}(X = 1) = \frac{1}{k_{kin}(1)} = \frac{1}{(0.11s^{-1})} = 9s.$$

At an intermediate point between these two extremes, for example at the equator where X = x/L = 0.5, we obtain:

$$\tau_{slow}(X = 0.5) = \frac{1}{k_{kin}(0.5)} = \frac{1}{(0.065s^{-1})} = 15s.$$

For the reverse transition, the mean time spent in the fast state for all X is given by:

$$\tau_{fast} = \frac{1}{k_{phos}} = \frac{1}{(0.1s^{-1})} = 10s$$

(this equation is valid for all X, as the rate of dephosphorylation is constant throughout the cytoplasm).

Using the diffusion coefficients, we can then compute the mean distance traveled in the fast and slow states. The root-mean-squared (rms) distance traveled by molecules in the slow state also depends on position. For simplicity as an intermediate case, let us use the value again at the cell midpoint (X = 0.5),

$$l_{slow}(0.5) = \sqrt{\frac{2D_A}{k_{kin}(0.5)}} = \sqrt{\frac{2(0.07\mu m^2/s)}{0.065s^{-1}}} = 1.5\mu m$$

and the rms distance traveled by fast molecules is

$$l_{fast} = \sqrt{\frac{2D_B}{k_{phos}}} = \sqrt{\frac{2(5.0\mu m^2/s)}{0.1s^{-1}}} = 10\mu m.$$

Thus, in the base case, a molecule will not typically be able to diffuse the entire length of the cell during one fast phase. Rather, it will switch multiple times to move from one end to the other, or even to move, e.g., from X = 3L/4 to X = L/4, a distance of L/2 = 25 μm as depicted in Figure S6A.

Because a molecule will switch multiple times, it is appropriate to approximate the diffusion process by a single effective diffusion coefficient defined here as

$$D_{eff} = fD_A + (1 - f)D_B \tag{17}$$

where f is the fraction of time spent in the slow state (i.e., a duty cycle for MEX-5), which is given by

$$f = \frac{\tau_{slow}(0.5)}{\tau_{slow}(0.5) + \tau_{fast}}. \tag{18}$$

This effective diffusion coefficient can then be used to calculate the time to travel half the length of cell (i.e., for a molecule to move from the midpoint of the posterior cytoplasm to the midpoint of the anterior cytoplasm), which is

$$\tau = \frac{\left(\frac{L}{2}\right)^2}{2D_{eff}}. \tag{19}$$

In the case of an initially uniform concentration profile, τ approximates the mean time for a molecule to move from posterior cytoplasm to anterior cytoplasm, and thereby begin to establish the emerging steady-state gradient along the AP axis.

For the base parameter set, we estimate

$$f = \frac{15s}{15s + 10s} = 0.6$$

meaning that near the equator, molecules spend about 60% of their time in the slow state, in agreement with experiment. From this value we can calculate the effective diffusion coefficient as

$$D_{eff} = (0.6)\left(0.07\frac{\mu m^2}{s}\right) + (0.4)\left(5\frac{\mu m^2}{s}\right) = 2\frac{\mu m^2}{s}$$

in agreement with experiment. Therefore, the time scale of gradient formation in the case of the base parameter set is

$$\tau = \frac{\left(50\frac{\mu m}{2}\right)^2}{2\left(2\frac{\mu m^2}{s}\right)} = 160s,$$

which is in good agreement with experiment and with the base case unsteady-state simulation. Therefore, the cytoplasmic model with the base parameter set explains the rapid formation of the gradient over a few minutes, as shown in Figure S5B.

Parameter Sensitivity Analysis: Cytoplasmic Model

To explore the extent of valid parameter space in the cytoplasmic model, we conducted a sensitivity analysis. In each perturbation described below, we first discuss the a priori expectation based on the time and length scales defined above.

Varying k_{phos} Alone (Figures S5C and S5D)

If k_{phos} were increased 10-fold, then molecules would spend relatively little time in the fast state compared to the base case. In this case

$$\tau_{fast} = 1s$$

and the majority of the time will be spent in the slow state so that

$$f = \frac{15s}{15s + 1s} = 0.94.$$

This will slow the effective diffusion so that

$$D_{eff} = (0.94)\left(0.07\frac{\mu m^2}{s}\right) + (0.06)\left(5.0\frac{\mu m^2}{s}\right) = 0.37\frac{\mu m^2}{s}$$

and the corresponding approach to steady-state will take on the order of

$$\tau = \frac{\left(50\frac{\mu m}{2}\right)^2}{2\left(0.37\frac{\mu m^2}{s}\right)} = 840s.$$

Thus, a gradient will form, but will take longer as shown in Figure S5C. The gradient is slightly weaker than the base case because the entire model hinges on the two diffusion coefficients being different. If they are the same, then no gradient forms at all. The larger the disparity between the two diffusion coefficients, the larger the gradient will be.

If k_{phos} were decreased 10-fold, then

$$\tau_{fast} = 100s$$

and the majority of the time will be spent in the fast state so that

$$f = \frac{15s}{15s + 100s} = 0.13.$$

This will speed up the effective diffusion so that

$$D_{eff} = (0.13)\left(0.07\frac{\mu m^2}{s}\right) + (0.87)\left(5.0\frac{\mu m^2}{s}\right) = 4.4\frac{\mu m^2}{s}$$

and the corresponding approach to steady-state will take on the order of

$$\tau = \frac{\left(50\frac{\mu m}{2}\right)^2}{2\left(4.4\frac{\mu m^2}{s}\right)} = 70s.$$

In this case, the gradient forms quickly but will be relatively flat due to the large fraction in the fast state and the long distances that fast molecules diffuse, which in this case is,

$$l_{fast} = 30\mu m.$$

Therefore, this case fails due to the lack of a gradient, as shown in Figure S5D.

Varying k_{kin} Alone (Figures S5E and S5F)

This case is identical to varying k_{phos} alone, except that increasing k_{kin} results in the same outcome as decreasing k_{phos}, and vice versa. Simulations confirm this interpretation, as shown in Figure S5E and S5F.

Varying k_{phos} and k_{kin} Coordinately (Figures S5G–S5I)

If k_{phos} and k_{kin} are varied coordinately, then the relative fractions of fast and slow are constant, and so the effective diffusion coefficient will not vary. For example, if both k_{phos} and k_{kin} are increased 10-fold, then neither the steady-state gradient nor the dynamic approach to steady-state should change. As shown in Figure S5G, simulations confirm this reasoning. However, if k_{phos} and k_{kin} are both decreased by 10-fold, then the times spent in each of the two states is 10-fold greater so that

$$\tau_{slow}(X = 0.5) = 150s$$

and

$$\tau_{fast} = 100s.$$

As a result, molecules will cover greater distances than in the base case,

$$l_{slow}(0.5) = 4.7\mu m$$

and

$$l_{fast} = 32\mu m$$

meaning that the assumption regarding effective diffusion, i.e., that molecules switch multiple times as they diffuse from end of the cell to the other, is starting to break down. As a result, the gradient should start to weaken, which is observed to be the case as shown in Figure S5H (note: the time scale was increased 10-fold to 6000 s because of the slow dynamics). If k_{phos} and k_{kin} are both decreased 100-fold, the effect becomes even more pronounced, and now even the slow molecule will diffuse over appreciable distances due to the slow kinase kinetics. In this case,

$$\tau_{slow}(X = 0.5) = 1500s$$

and

$$\tau_{fast} = 1000s.$$

As a result, molecules will cover distances approaching, or exceeding, the length of the embryo (L = 50 μm),

$$l_{slow}(0.5) = 15\mu m$$

and

$$l_{fast} = 100\mu m.$$

Not only does this effectively destroy the gradient, it also takes a very long time for the gradient to form, as the kinetics are limiting. In this case the approach to steady-state will take > 1000 s (17 min), far longer than observed experimentally. These dynamics were confirmed in simulation, as shown in Figure S5I (note: the time scale was increased 10-fold to 6000 s because of the slow dynamics).

Varying DA and DB (Figures S5J–S5L)

The only remaining parameters in the cytoplasmic model are the diffusion coefficients, D_A and D_B. As mentioned at above, the values of D_A and D_B must be quite different from each other in order for the gradient to form at all.

We first consider the effect of varying the slow diffusion coefficient, D_A. If D_A were increased 10-fold, then the effective diffusion coefficient will change only modestly,

$$D_{eff} = (0.6)\left(0.7\frac{\mu m^2}{s}\right) + (0.4)\left(5\frac{\mu m^2}{s}\right) = 2.4\frac{\mu m^2}{s}$$

which is an increase of only 20%. Note that in the regime where the model works, i.e., where $D_A << D_B$, the effective diffusion coefficient is dominated by the fraction of time spent in the slow state, f, and the fast diffusion coefficient, D_B,

$$D_{eff} \approx (1 - f)D_B. \quad (20)$$

Thus, the gradient should be slightly weaker due to the increased slow diffusion coefficient, but the approach to the steady-state should be on the same time scale as the base case, as confirmed in Figure S5J.

In the opposite case of a 10-fold lower value, the gradient should be steeper, due to the increased disparity between the fast and slow diffusion coefficients. However, the effect should only be slight because even in the base case, the disparity is already large: i.e., $D_B/D_A = 70$. Increasing the ratio further to $D_B/D_A = 700$, as in the case of decreasing D_A 10-fold, should increase the steepness of the gradient only modestly. The effect on dynamics in also modest, as the effective diffusion coefficient is insensitive to the slow diffusion coefficient. In this case,

$$D_{eff} = (0.6)\left(0.007\frac{\mu m^2}{s}\right) + (0.4)\left(5\frac{\mu m^2}{s}\right) = 2.0\frac{\mu m^2}{s}.$$

Thus, the model is insensitive to 10-fold changes in the slow diffusion coefficient, D_A. These behaviors are documented in Figures S5J and S5K.

Increasing the fast diffusion coefficient by 10-fold will only serve to steepen the gradient, although again this will only increase an already large disparity between fast and slow diffusion coefficients and the effect should be modest. A stronger effect will be in the unsteady-state dynamics, which should proceed according to

$$D_{eff} = (0.6)\left(0.07\frac{\mu m^2}{s}\right) + (0.4)\left(50.0\frac{\mu m^2}{s}\right) = 20\frac{\mu m^2}{s}$$

and the corresponding approach to steady-state will take on the order of

$$\tau = \frac{\left(50\frac{\mu m}{2}\right)^2}{2\left(20\frac{\mu m^2}{s}\right)} = 16s.$$

However, it is important to note that this time scale is approaching the time scale of the slow state (τ_{slow} = 15 s), so that the approach to steady-state will be limited by both the kinase reaction and subsequent diffusion in the fast state.

Decreasing D_B by 10-fold will slightly weaken the gradient, due to the modest lessening of the disparity between the fast and slow diffusion coefficients as discussed above for varying D_A. However, the approach to steady-state should slow significantly due to dependence of the effective diffusion coefficient on the slow diffusion coefficient. Quantitatively, D_{eff} is reduced to

$$D_{eff} = (0.6)\left(0.07\frac{\mu m^2}{s}\right) + (0.4)\left(0.5\frac{\mu m^2}{s}\right) = 0.24\frac{\mu m^2}{s}$$

so that

$$\tau = \frac{\left(50\frac{\mu m}{2}\right)^2}{2\left(0.24\frac{\mu m^2}{s}\right)} = 1300s.$$

Thus, the gradient will be weak and slow to reach steady-state. The effect of changing D_B is shown in Figures S5L and S5M, and the effects predicted are observed in the simulation.

Parameter Sensitivity Analysis: Cortical Model (Figures S6A–S6F)

The steady-state behavior of the cortical model has been discussed extensively in Lipkow and Odde (2008). In the present study, two assumptions were altered from those in the previous study: (1) the kinase was moved from the left boundary to the right boundary, and (2) the kinase generates the fast state instead of the slow state. However, these changes do not fundamentally alter the model, only the nomenclature. Fundamentally, the cortical model is invalidated by the observation that elimination of cortical PAR-1 does not eliminate the MEX-5 gradient (Figure 2D). Nevertheless, for completeness we consider some of the quantitative aspects of the cortical model and point out additional shortcomings of this model. It is important to note that the fundamental idea of the original model still underlies the cytoplasmic model to explain the MEX-5 gradient: spatially segregated kinase-phosphatase reactions will generate a *steady-state total protein concentration gradient of their substrate*, provided the diffusion coefficients of the phosphorylated and dephosphorylated species differ appreciably.

For the cortical model to work in the case of MEX-5, the kinase reaction at the right boundary (X = 1) needs to be rapid, so that the concentration of the slow species at the boundary, $c_A(X = 1)$ is nearly zero. This creates an AP gradient in the slow species, as observed experimentally. As the fast species is generated at X = 1, it rapidly diffuses away to create a nearly uniform concentration of B within the cytoplasm, as depicted in Figure S6A. Summed together, the two gradients form a total protein concentration gradient as described previously in Lipkow and Odde.

If we use the base case value for k_{phos} from the cytoplasmic model, $k_{phos} = 0.1\ s^{-1}$, and constrain D_A and D_B to be the experimentally obtained values (0.07 $\mu m^2/s$ and 5.0 $\mu m^2/s$, respectively), then the resulting steady-state total protein concentration gradient is appreciable, although only near the posterior pole at X = 1 (Figure S6B). The gradient length can be increased to extend further into the anterior cytoplasm (X < 0.5) by decreasing the rate of the phosphatase reaction. For example, if $k_{phos} = 0.01\ s^{-1}$, then better agreement is achieved with the observed steady-state gradient extending over the length of the embryo (Figure S6C). Although this gradient is reasonable, it requires that almost all of the protein be in the slow state, which is inconsistent with experimental observation.

To approximate the observed relative ratios of slow:fast (~2:1 in anterior cytoplasm, ~1:1 in posterior cytoplasm), the phosphatase rate needs to be very slow, comparable to the kinase rate. The kinase rate is in turn diffusion-limited by the time it takes for molecules in the slow state to diffuse to the right boundary at X = 1. As shown in Figure S6D, when the phosphatase rate is decreased to $k_{phos} = 0.0001\ s^{-1}$, we find reasonable ratios of slow:fast.

Although the cortical model can give rise to the observed total protein gradient, the time scale of approach to steady-state is limited by the rate at which the slow molecules can diffuse to the right boundary. Using a minimum gradient length of L/4 (i.e., the distance from X = 3L/4, the midpoint of the posterior cytoplasm, to the right boundary at X = 1), we obtain a time scale for approach to steady-state of

$$\tau = \frac{\left(\frac{L}{4}\right)^2}{2(D_A)} = \frac{\left(50\frac{\mu m}{4}\right)^2}{2\left(0.07\frac{\mu m^2}{s}\right)} = 1100\text{s}.$$

Note that the rate of approach to steady-state should be insensitive to the phosphatase rate constant, k_{phos}, and instead will depend on the slow diffusion coefficient, D_A, which we confirmed occurs in the simulations as shown in Figures S6E and S6F.

Thus, the cortical model has the following difficulties: (1) it cannot account for the experimentally observed MEX-5 gradient that develops in the absence of cortical PAR-1, and (2) it requires a slower approach to steady-state than observed experimentally. In particular, it predicts a half-time for gradient formation (~1000 s = ~17 min) that occurs ~5 min after NEBD. By contrast, the cytoplasmic model accounts for both of these observations, and all other observations so far as described above.

SUPPLEMENTAL REFERENCES

Aono, S., Legouis, R., Hoose, W.A., and Kemphues, K.J. (2004). PAR-3 is required for epithelial cell polarity in the distal spermatheca of C. elegans. Development *131*, 2865–2874.

Berg, H.C. (1993). Random Walks in Biology, Expanded Edition edn (Princeton, New Jersey: Princeton University Press).

Cheeseman, I.M., Niessen, S., Anderson, S., Hyndman, F., Yates, J.R., 3rd, Oegema, K., and Desai, A. (2004). A conserved protein network controls assembly of the outer kinetochore and its ability to sustain tension. Genes Dev. *18*, 2255–2268.

Daniels, B.R., Dobrowsky, T.M., Perkins, E.M., Sun, S.X., and Wirtz, D. (2010). MEX-5 enrichment in the C. elegans early embryo mediated by differential diffusion. Development *137*, 2579–2585.

Froment, G.F., and Bischoff, K.B. (1990). Chemical Reactor Analysis and Design, Second Edition (New York, NY: John Wiley & Sons, Inc.).

Gallo, C.M., Wang, J.T., Motegi, F., and Seydoux, G. (2010). Cytoplasmic partitioning of P granule components is not required to specify the germline in C. elegans. Science *330*, 1685–1689.

Guo, S., and Kemphues, K.J. (1995). par-1, a gene required for establishing polarity in C. elegans embryos, encodes a putative Ser/Thr kinase that is asymmetrically distributed. Cell *81*, 611–620.

Gönczy, P., Bellanger, J.M., Kirkham, M., Pozniakowski, A., Baumer, K., Phillips, J.B., and Hyman, A.A. (2001). zyg-8, a gene required for spindle positioning in C. elegans, encodes a doublecortin-related kinase that promotes microtubule assembly. Dev. Cell *1*, 363–375.

Hundley, H.A., Krauchuk, A.A., and Bass, B.L. (2008). C. elegans and H. sapiens mRNAs with edited 3′ UTRs are present on polysomes. RNA *14*, 2050–2060.

Lai, W.S., Kennington, E.A., and Blackshear, P.J. (2002). Interactions of CCCH zinc finger proteins with mRNA: non-binding tristetraprolin mutants exert an inhibitory effect on degradation of AU-rich element-containing mRNAs. J. Biol. Chem. *277*, 9606–9613.

Merritt, C., Rasoloson, D., Ko, D., and Seydoux, G. (2008). 3′ UTRs are the primary regulators of gene expression in the C. elegans germline. Curr. Biol. *18*, 1476–1482.

Meyers, J., Craig, J., and Odde, D.J. (2006). Potential for control of signaling pathways via cell size and shape. Curr. Biol. *16*, 1685–1693.

Praitis, V., Casey, E., Collar, D., and Austin, J. (2001). Creation of low-copy integrated transgenic lines in *Caenorhabditis elegans.* Genetics *157*, 1217–1226.

Redemann, S., Pecreaux, J., Goehring, N.W., Khairy, K., Stelzer, E.H., Hyman, A.A., and Howard, J. (2010). Membrane invaginations reveal cortical sites that pull on mitotic spindles in one-cell C. elegans embryos. PLoS ONE *5*, e12301.

Schubert, C.M., Lin, R., de Vries, C.J., Plasterk, R.H., and Priess, J.R. (2000). MEX-5 and MEX-6 function to establish soma/germline asymmetry in early C. elegans embryos. Mol. Cell *5*, 671–682.

Severson, A.F., and Bowerman, B. (2003). Myosin and the PAR proteins polarize microfilament-dependent forces that shape and position mitotic spindles in *Caenorhabditis elegans.* J. Cell Biol. *161*, 21–26.

Stitzel, M.L., Pellettieri, J., and Seydoux, G. (2006). The C. elegans DYRK kinase MBK-2 marks oocyte proteins for degradation in response to meiotic maturation. Curr. Biol. *16*, 56–62.

Tenlen, J.R., Molk, J.N., London, N., Page, B.D., and Priess, J.R. (2008). MEX-5 asymmetry in one-cell C. elegans embryos requires PAR-4- and PAR-1-dependent phosphorylation. Development *135*, 3665–3675.

Timmons, L., and Fire, A. (1998). Specific interference by ingested dsRNA. Nature *395*, 854.

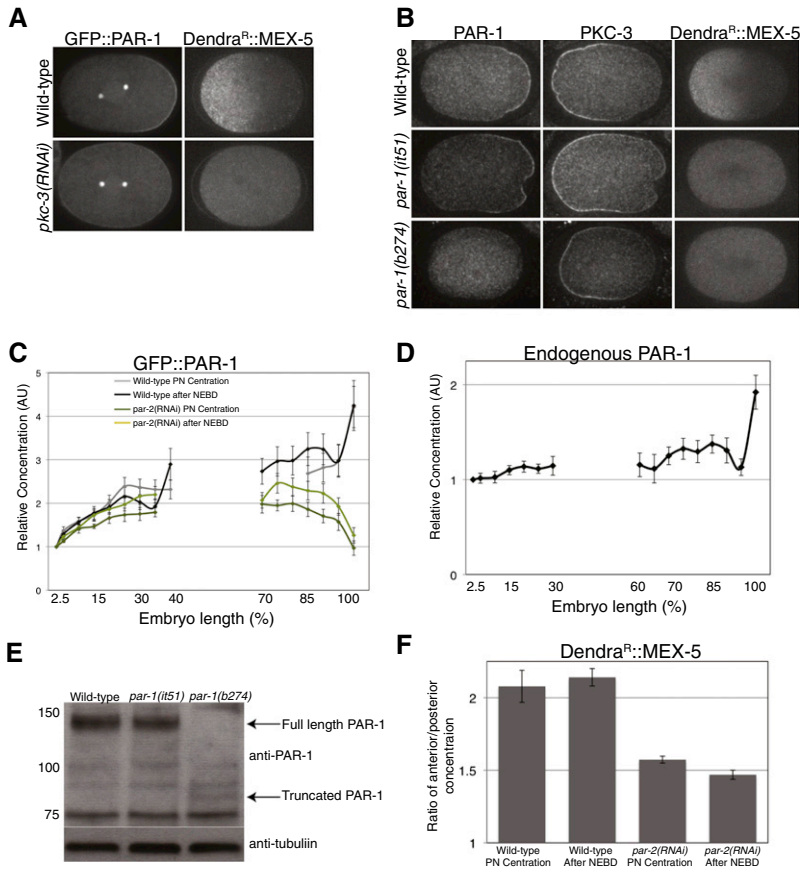

Figure S1. The Enrichment of PAR-1 on the Posterior Cortex Is Disrupted in *pkc-3(RNAi)*, *par-2(RNAi)*, and *par-1(b274)* Zygotes, Related to Figure 2

(A) Single-plane confocal images of wild-type and *pkc-3 (RNAi)* embryos expressing GFP::PAR-1 or Dendra::MEX-5. Note that in *pkc-3(RNAi)* embryos, PAR-1 localizes throughout the cortex and cytoplasm and Dendra^R::MEX-5 is evenly distributed throughout the cytoplasm. PAR-1 also localizes on centrosomes (bright dots) as reported previously (Gönczy et al., 2001).

(B) Single-plane confocal images of zygotes of the indicated genotypes immunostained with antibodies against PKC-3 (Aono et al., 2004) and PAR-1 (Guo and Kemphues, 1995) or expressing Dendra::MEX-5. PKC-3 is enriched on the anterior cortex in all genotypes.

(C) Quantification of the GFP::PAR-1 concentration gradient in wild-type and *par-2 (RNAi)* zygotes at pronuclear centration (pronuclei have met at the center of the embryo) and after NEBD. GFP::PAR-1 concentration was determined for multiple embryos (between 7 and 15) at regular positions along the long axis. Obtaining accurate scale measurements is complicated by the fact that GFP::PAR-1 levels approach autofluorescence levels in the anterior cytoplasm. To correct for the background signal from autofluorescence, autofluorescence was measured in embryos not expressing GFP (n = 8) and subtracted from GFP::PAR-1 values. GFP::PAR-1 levels are expressed as the mean concentration relative to the concentration at 2.5% embryo length (normalized to 1 for each embryo). Values between 45% and 65% embryo length were omitted because of signal distortion caused by accumulation of GFP::PAR-1 on centrosomes in this region. Error bars represent SEM.

(D) Quantification of endogenous PAR-1 levels in wild-type embryos. Ten mitotic stage embryos were stained with anti-PAR-1 antibody (Guo and Kemphues, 1995) and imaged at the midplane of the cell. Fluorescence levels are expressed as the mean concentration relative to the concentration at 2.5% embryo length (normalized to 1 for each embryo). Values between 35% and 55% embryo length were omitted because of signal distortion caused by the presence of pronuclei and the accumulation of PAR-1 on centrosomes. Unlike the GFP::PAR-1 quantification in panel C, background cytoplasmic staining (Guo and Kemphues, 1995) has not been subtracted from these values. This likely results in the apparently weaker enrichment of endogenous PAR-1 in the posterior cytoplasm relative to GFP::PAR-1. In an additional 10 out of 12 embryos (not included in this quantification), PAR-1 levels were higher in the posterior cytoplasm compared to the anterior cytoplasm. Error bars represent SEM.

(E) Western blot analysis of PAR-1 in wild-type, *par-1(it51)* and *par-1(b274)* worms. Extracts from approximately 130 hermaphrodites were separated on SDS-PAGE gels and probed with anti-PAR-1 (Guo and Kemphues, 1995) and anti-tubulin antibodies (mouse anti-tubulin monoclonal DM1A, Sigma-Aldrich). Position of molecular weight markers are indicated on the left. *par-1(b274)* worms lack full-length PAR-1 and express instead a truncated form (~86 kDa) (Hurd and Kemphues, 2003) at 14% of wild-type levels.

(F) Concentration ratio of anterior to posterior Dendra^R::MEX-5 in wild-type and *par-2(RNAi)* embryos at pronuclear centration and following NEBD. Note that Dendra^R::MEX-5 asymmetry at pronuclear centration is reduced in *par-2(RNAi)* embryos compared to wild-type and weakens further following NEBD. This is consistent with the weaker PAR-1 gradient that forms by pronuclear meeting in *par-2(RNAi)* embryos and its decay after NEBD (panel C). Error bars represent SEM.

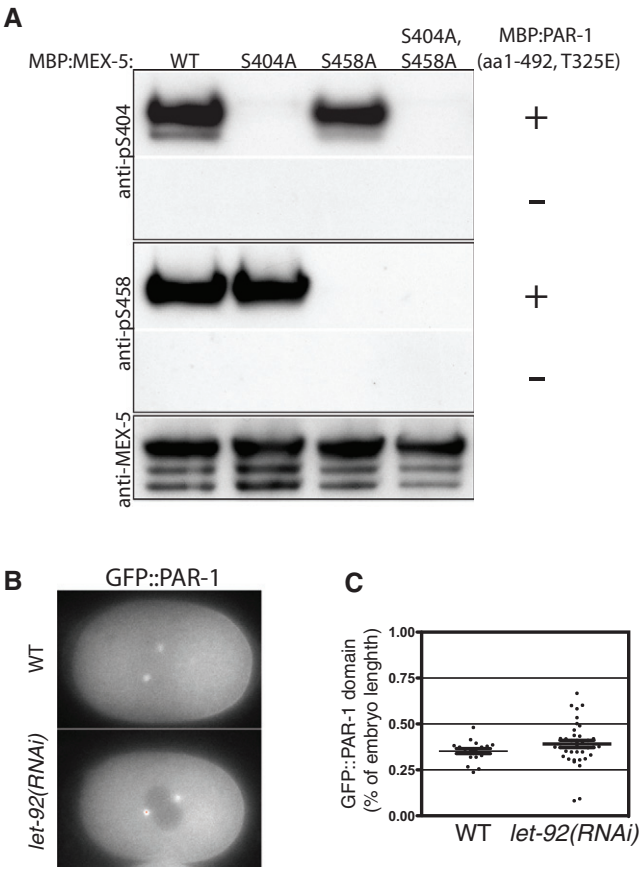

Figure S2. Specificity of MEX-5 (pS404) and MEX-5 (pS458) Antibodies and PAR-1 Localization in *let-92(RNAi)* Zygotes, Related to Figure 3

(A) Western blot demonstrating the specificity of the anti-MEX-5 (pS404) and anti-MEX-5 (pS458) phosphospecific antibodies: western blot analysis of samples from in vitro kinase reactions using fusion proteins partially purified from *E. coli*. MBP::MEX-5 fusion proteins containing the indicated substitutions were incubated with or without MBP::PAR-1(aa 1–492, T325E). Samples were separated by SDS PAGE and probed with antibodies against MEX-5, MEX-5 (pS404), and MEX-5 (pS458).

(B) Confocal micrographs of GFP::PAR-1 localization in wild-type and *let-92 (RNAi)* embryos. GFP::PAR-1 segregates to the posterior of *let-92 (RNAi)* embryos as it does in wild-type.

(C) Cortical PAR-1 domain expressed as a percentage of total embryo length in wild-type (WT) and *let-92(RNAi)* embryos. The variability in PAR-1 domain size in *let-92(RNAi)* embryos is due to the occasional embryo with an off-axis GFP::PAR-1 domain, but PAR-1 was asymmetric in all embryos examined.

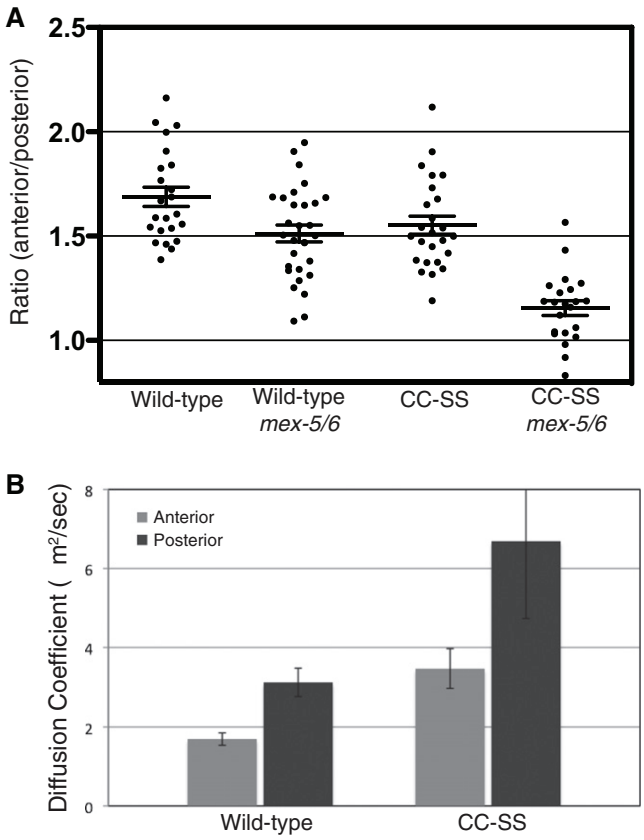

Figure S3. The Gradient Formed by MEX-5 (C286S,C292S,C331S,C337S) Depends on Endogenous MEX-5 and MEX-6, Related to Figure 4

(A) Ratio of anterior to posterior concentration of Dendra^{R}::MEX-5 and Dendra^{R}::MEX-5 (C286S,C292S,C331S,C337S) (denoted CC-SS in graph) in wild-type embryos and *mex-5(zu199); mex-6(RNAi)* embryos at NEBD. C286S, C292S,C331S, C337S are mutations that replace the first two zinc-coordinating cysteines in each finger and are predicted to disrupt folding of the fingers and RNA binding (Lai et al., 2002). Unlike other MEX-5 fusions in this study, which are driven by the *mex-5* promoter, these fusions were driven by the weaker *pie-1* promoter. We attempted to generate Dendra::MEX-5(C286S,C292S,C331S,C337S) driven by the higher-expressing *mex-5* promoter but were not able to recover lines raising the possibility that this fusion is toxic at higher expression levels. As in Tenlen et al. (2008), we were able to recover lines driven by the weaker *pie-1* promoter and found that Dendra^{R}::MEX-5 (C286S,C292S,C331S,C337S) formed a gradient similar to that seen with wild-type Dendra^{R}::MEX-5. As shown here, however, the Dendra^{R}::MEX-5 (C286S,C292S,C331S,C337S) gradient is dependent on endogenous MEX-5 and its homolog MEX-6. In *mex-5(zu199); mex-6(RNAi)* zygotes, Dendra^{R}:MEX-5(C286S,C292S,C331S,C337S) formed at most a weak gradient.

(B) Apparent diffusion coefficients of Dendra^{R}::MEX-5 mutants measured at NEBD (after polarization) in the presence of endogenous MEX-5 and MEX-6. Dendra^{R}::MEX-5 (C286S,C292S,C331S,C337S) diffuses approximately twice as fast as Dendra^{R}::MEX-5, consistent with a defect in anchoring. We conclude that the RNA binding domain of MEX-5 restricts mobility, and that interactions among MEX-5 and MEX-6 molecules may also influence mobility.

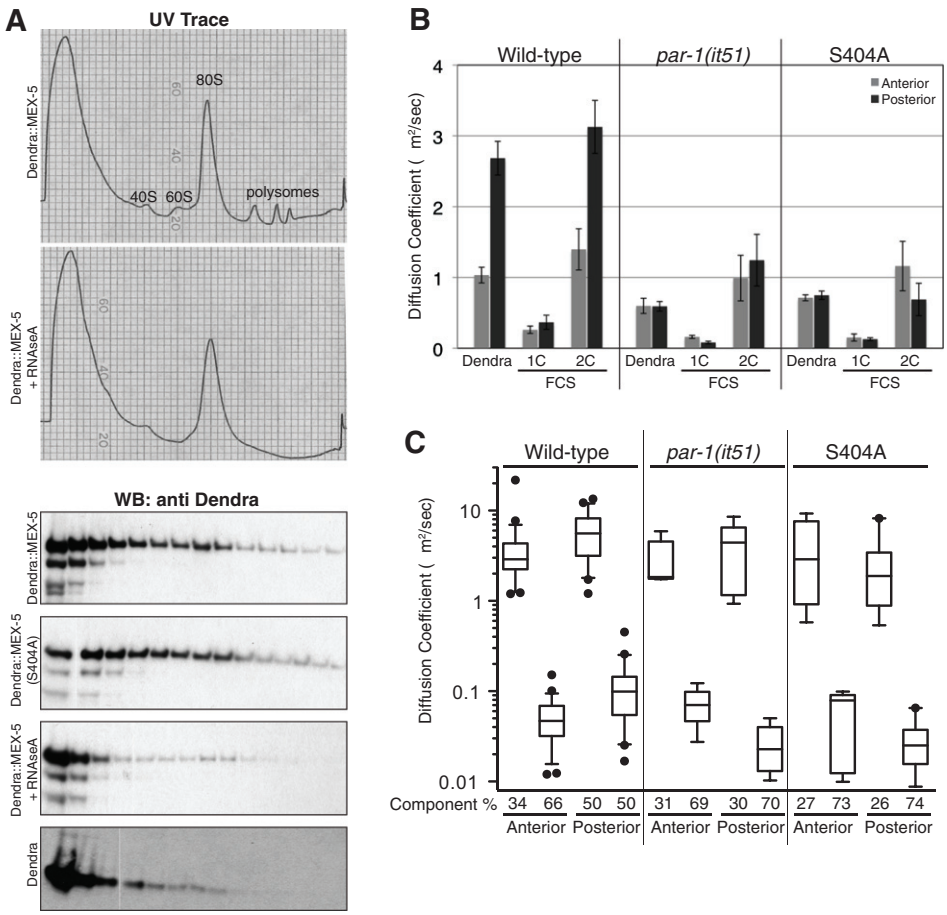

Figure S4. MEX-5 Associates with Multiple Complexes In Vivo, Related to Figure 5

(A) Representative UV traces and western blots following sucrose gradient fractionation of whole worm extracts with or without RNaseA treatment from transgenic worms expressing Dendra::MEX-5. UV traces were generated by flowing gradients through a UV detector (described in the Experimental Procedures) during fraction collection. The position of polysomes, 40S, 60S, and 80S ribosomal subunits are indicated. Note that the relatively mild RNase treatment eliminates polysomes but preserves 80S subunits. Photoshop was used to crop out lanes containing protein standards from the western blots.

(B) Comparison of apparent MEX-5 diffusion coefficients determined using photoconversion of Dendra^{R}::MEX-5 or using FCS on GFP::MEX-5 and fitting the spectra to one or two-component models. For two-component FCS models, population diffusion coefficients were calculated as the weighted average of fast and slow-diffusing components. One-component FCS models yielded diffusion coefficients that were significantly lower than those determined experimentally with Dendra^{R}::MEX-5. In contrast, two-component models fit the Dendra^{R}::MEX-5 values well. The Dendra^{R}::MEX-5 diffusion coefficients are also presented in Figures 2C and 2D. Error bars represent SEM.

(C) Box and whiskers plot of diffusion coefficients of GFP::MEX-5 complexes as calculated by FCS analysis. The boxes contain the 25th to 75th percentile and the whiskers contain 10-90th percentile. Data points outside the 10-90th percentile are plotted as individual points. Note that in all measurements, both fast and slow components were detected, with ~100-fold difference in diffusion. The mean percentage of each component is indicated below the graph and is also presented in Figure 5B. Three-component models (analyzed between time lags 7.2 μs and 3.35 s as used for one- and two-component models) yielded a similar range of average diffusion coefficient values (anterior = .038, 0.41, and 5.15 μm^2/s; posterior = 0.028, 0.45 and 8.04 μm^2/s). A three-component model analyzed between the time lags 16 μs and 184 ms as used by Daniels et al. (2010) again yielded a similar range of average diffusion coefficients (anterior = .032, 0.48, and 5.59 μm^2/sc; posterior = 0.030, 0.60, and 9.51 μm^2/s). In all cases, the slowest-diffusing component was no less than 35% of total in the posterior cytoplasm and 43% of total in the anterior cytoplasm. We conclude that including the slow component is important when constructing models of MEX-5 diffusion.

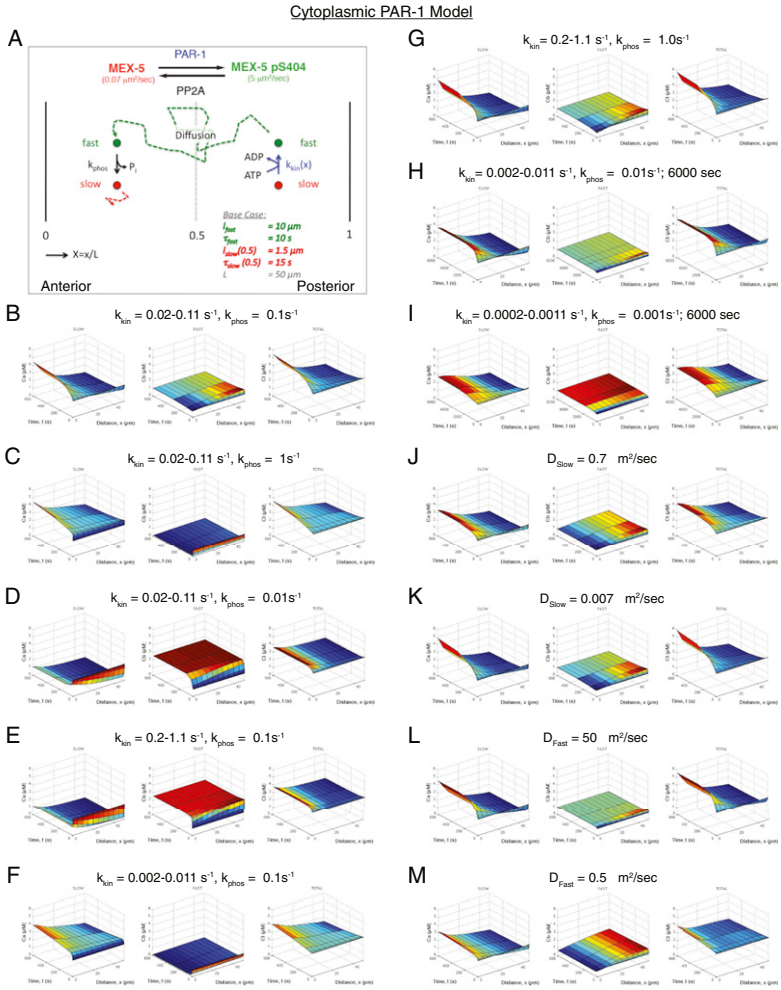

Figure S5. Unsteady-State Analysis of Cytoplasmic PAR-1 Model, Related to Figure 6

(A) Schematic of the cytoplasmic PAR-1 model using the base parameters. In this model, the transitions of MEX-5 between the phosphorylated, fast-diffusing form (depicted by a green circle) and the dephosphorylated, slow-diffusing form (depicted by a red circle) is controlled by PAR-1 and PP2A. PAR-1 activity is in an anterior/low to posterior/high linear cytoplasmic gradient. Phosphatase activity is uniform in the cytoplasm. Because k_{phos} is uniform, the mean time spent in the fast state (τ_{fast}) and the root-mean-squared distance traveled by the fast (l_{fast}) species are uniform throughout the cell. In contrast, the mean time spent in the slow state (τ_{slow}) and the root-mean-squared distance traveled by the slow species (l_{slow}) varies along the A/P axis. The length of the embryo (L) is 50 μm and the values for l_{fast}, τ_{fast}, l_{slow}, and τ_{slow} at midpoint of the cell (X = 0.5) are shown. See the Extended Experimental Procedures for a discussion of the contribution of different parameters to the cytoplasmic PAR-1 model.

(B) Graphs showing the results of a 600 s simulation of the cytoplasmic PAR-1 model with the base set of parameters: cytoplasmic PAR-1 activity gradient (k_{kin} = 0.02–0.11 s^{-1}), uniform phosphatase activity (k_{phos} = 0.1 s^{-1}), D_{Slow} = 0.07 $\mu m^2/s$, and D_{Fast} = 5.0 $\mu m^2/s$. The concentrations of the slow MEX-5 species (C_a, left graph), the fast MEX-5 species (C_b, middle graph), and total MEX-5 (C_t, right graph) are plotted against time (in seconds) and distance along the anterior/posterior axis (anterior, x = 0 μm; posterior, x = 50 μm). Concentration is coded by a rainbow scale in which red represents maximum and blue represents minimum concentration for each species within each simulation. At t = 0, 70% of MEX-5 is in the slow state and 30% of MEX-5 is in the fast state.

(C) The effect of increasing phosphatase activity 10-fold (k_{phos} = 1 s^{-1}).

(D) The effect of decreasing phosphatase activity 10-fold (k_{phos} = 0.01 s^{-1}).

(E) The effect of increasing kinase activity 10-fold (k_{kin} = 0.2–1.1 s^{-1}).

(F) The effect of decreasing kinase activity 10-fold (k_{kin} = 0.002-0.011 s^{-1}).

(G) The effect of increasing kinase and phosphatase activity 10-fold (k_{kin} = 0.2–1.1 s^{-1}, k_{phos} = 1 s^{-1}).

(H) The effect of decreasing kinase and phosphatase activity 10-fold (k_{kin} = 0.002–0.011 s^{-1}, k_{phos} = 0.01 s^{-1}). Note that this simulation was run for 6000 s because of the slow reaction kinetics.

(I) The effect of decreasing kinase and phosphatase activity 100-fold (k_{kin} = 0.0002–0.0011 s^{-1}, k_{phos} = 0.001 s^{-1}). Note that this simulation was run for 6000 s because of the slow reaction kinetics.

(J) The effect of increasing the diffusivity of the slow MEX-5 species 10-fold (D_{slow} = 0.7 $\mu m^2/s$).

(K) The effect of decreasing the diffusivity of the slow MEX-5 species 10-fold (D_{slow} = 0.007 $\mu m^2/s$).

(L) The effect of increasing the diffusivity of the fast MEX-5 species 10-fold (D_{fast} = 50 $\mu m^2/s$).

(M) The effect of decreasing the diffusivity of the fast MEX-5 species 10-fold (D_{fast} = 0.5 $\mu m^2/s$).

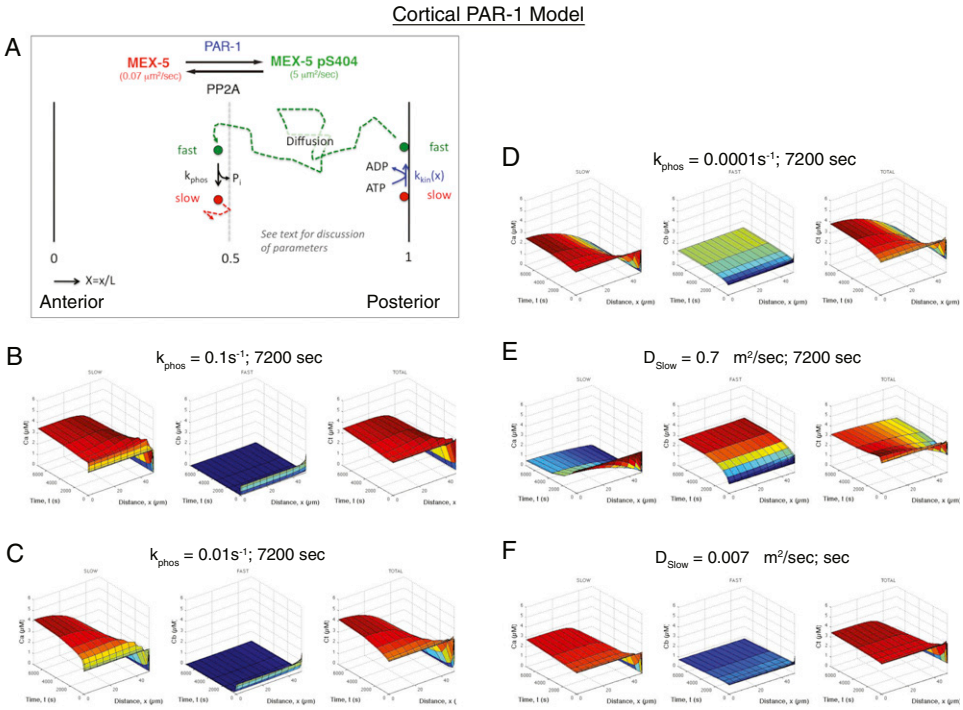

Figure S6. Unsteady-State Analysis of Cortical PAR-1 Model, Related to Figure 6

(A) Schematic of the cortical PAR-1 model. As in the cytoplasmic PAR-1 model, the transition of MEX-5 between the phosphorylated, fast-diffusing form (depicted by a green circle) and the dephosphorylated, slow-diffusing form (depicted by a red circle) is controlled by PAR-1 and PP2A. Phosphatase activity is uniform in the cytoplasm. PAR-1 activity is restricted to the posterior cortex and is assumed to be instantaneous in order to maximize its potential affect on MEX-5. See the Extended Experimental Procedures for a discussion of the contribution of different parameters to the cortical PAR-1 model.

(B) Cortical PAR-1 model with $k_{phos} = 0.1\ s^{-1}$. Note that in this and all subsequent panels in this Figure, the simulation was run for 7200 s because of the slow dynamics.

(C) The effect of decreasing phosphatase activity 10-fold ($k_{phos} = 0.01\ s^{-1}$).

(D) The effect of decreasing phosphatase activity 1000-fold ($k_{phos} = 0.0001\ s^{-1}$).

(E) The effect of increasing diffusivity of the slow MEX-5 species 10-fold ($D_{slow} = 0.7\ \mu m^2/s$).

(F) The effect of decreasing diffusivity of the slow MEX-5 species 10-fold ($D_{slow} = 0.007\ \mu m^2/s$).